EXPERIMENTAL INVESTIGATION ON STEAM-WATER DIRECT CONTACT CONDENSATION USING LASER-INDUCED FLUORESCENCE (LIF)

A Thesis

by

KIMOON LEE

Submitted to the Office of Graduate and Professional Studies of
Texas A&M University
in partial fulfillment of the requirements for the degree of

MASTER OF SCIENCE

Chair of Committee,	Yassin A. Hassan
Committee Members,	Kalyan Annamalai
	Rodolfo Vaghetto
	Duy Thien Nguyen
Head of Department,	John E. Hurtado

August 2019

Major Subject: Nuclear Engineering

ABSTRACT

The objective of this study is to conduct the experiments in the steam-water direct contact condensation and to investigate on the heat transfer characteristic such as the heat transfer coefficient, the pool temperature distribution and the bubble equivalent diameter using the laser-induced fluorescence (LIF) and the image processing technique. As a working fluid, deionized (DI) water purified by the reverse osmosis method is utilized. The experiments are performed at pool temperatures of 70-95°C ± 1°C, with different steam mass fluxes of 5-65 $kg/m^2 \cdot s$ on a 9.525 mm nozzle. The pool temperature is measured using the LIF and thermocouples, and the surface area of the bubble and the volume flow rate are calculated by the imaging processing technique. The averaged heat transfer coefficient is evaluated in a range of 24.57-179.78 $kW/m^2 \cdot K$. It is found that the heat transfer coefficient in unstable condensation region has high sensitivity on both the pool temperature and the steam mass flux. Using LIF method, the time-averaged temperature field of the entire pool is visualized, which could be utilized to evaluate not only the averaged heat transfer coefficient but also the local heat transfer coefficient since it is possible to measure the instantaneous local temperature change that could not be measured using thermocouples only. The bubble equivalent diameter is found in range of 0.033-0.114 m. The analysis on the change in the pattern of the bubble equivalent diameter due to increase of the steam mass flux and the pool temperature shows that the unstable isolated bubble occurred at the low mass flux region gradually tends to transform to the stable jet shape since the regime of the steam condensation is changed from the unstable condensation to the stable condensation as the steam mass flux increases.

DEDICATION

I dedicate this thesis to my lovely wife, Eunkyung, and my adorable sons, Dowon and Siwon. Without their support and encouragement, this work would not have been completed.

ACKNOWLEDGEMENTS

I would like to thank my committee chair, Dr. Yassin A. Hassan, for providing me with this great research and academic environment. I would also like to thank my committee members, Dr. Kalyan Annamalai, Dr. Rodolfo Vaghetto, and Dr. Thien Nguyen.

I would like to give special thanks to Joseph Seo who helped and guided the study of nuclear engineering. Also, I sincerely thank Dr. Se Ro Yang who gave me the opportunity to work on a great experiment with his valuable mentorship.

Finally, I really appreciate all my friends, colleagues, department faculties, and staffs for allowing me to spend a great time at Texas A&M University.

CONTRIBUTORS AND FUNDING SOURCES

This work was supported by a dissertation committee consisting of Professor Yassin A. Hassan, my advisor, and Professor Rodolfo Vaghetto and Professor Thien Nguyen of the Department of Nuclear Engineering, and Professor Kalyan Annamalai of the Department of Mechanical Engineering.

The experiments have been conducted with Arturo Cabral, Joseph Seo, and Dr. Se Ro Yang who have studied together in the thermal hydraulics laboratory advised by Dr. Hassan, Dr. Vaghetto, and Dr. Nguyen at Texas A&M University. The MATLAB codes utilized to analyze the experimental data were developed by Arturo Cabral and Dr. Se Ro Yang. All other works conducted for the dissertation were completed by me independently.

All my graduate study has been supported by a scholarship from the Republic of Korea Air Force.

NOMENCLATURE

A	Surface area of steam bubble, m^2
A_b	Wetted surface area of bubble, m
B	Condensation driving potential, $c_p\left(T_s - T_f\right)/\left(h_s - h_f\right)$
C	Dye concentration, kg/m^3
c_{PL}	Liquid specific heat, J/kg·K
c_{PS}	Steam specific heat, J/kg·K
d	Nozzle diameter, mm
$D_{b,eq}$	Bubble equivalent diameter of wetted surface, m
G	Steam mass flux, $kg/m^2 \cdot s$
G_m	Mean value of steam mass flux, $kg/m^2 \cdot s$
h_H	Convective heat transfer coefficient, $W/m^2 \cdot K$
h_s	Steam enthalpy, kJ/kg
h_f	Water in pool enthalpy, kJ/kg
h_{fg}	Enthalpy difference between steam and water in pool, J/kg
I	Fluorescence emission intensity, W/m^2
I_0	Incident laser beam intensity, W/m^2
$\dot{m}$	Steam flow rate, kg/s
P_L	Liquid pressure, kPa

P_s	Steam pressure, kPa
q	Heat transfer rate from steam to water, W
q''	Heat flux, W/m^2
T_f	Pool temperature, °C
T_s	Steam temperature, °C
ΔT	Temperature difference between steam and water in pool, °C
$\dot{V}$	Condensed volumetric flow rate of steam, m^3/s,
ρ_s	Steam density, kg/m^3
ρ_L	Liquid density, kg/m^3
ϕ	Fluorescence quantum efficiency
ε	Absorption coefficient, m^3/kg
λ_L	Liquid thermal conductivity, W/m·K
ν_L	Liquid kinematic viscosity, m^2/s

TABLE OF CONTENTS

Page

LIST OF FIGURES

Page

LIST OF TABLES

Page

1. INTRODUCTION

The steam-water direct contact condensation is one of the common phenomena occurring in a variety of industrial applications like a direct contact heat exchanger and a feedwater heater. Especially, this phenomenon has been used for various equipment of nuclear power plants such as an in-containment refueling water storage tank (IRWST) of the advanced pressurized water reactor (APWR) and a pressure suppression pool of the boiling water reactor (BWR) because of its high efficiency regarding heat transfer. In case of a loss of coolant accident (LOCA), BWRs utilizes pressure suppression pools to minimize the pressure increase inside the containment. A mixture (water, air, and steam) leaked from a break point of a cooling system is condensed directly in the suppression pool and vented as shown in Figure 1.

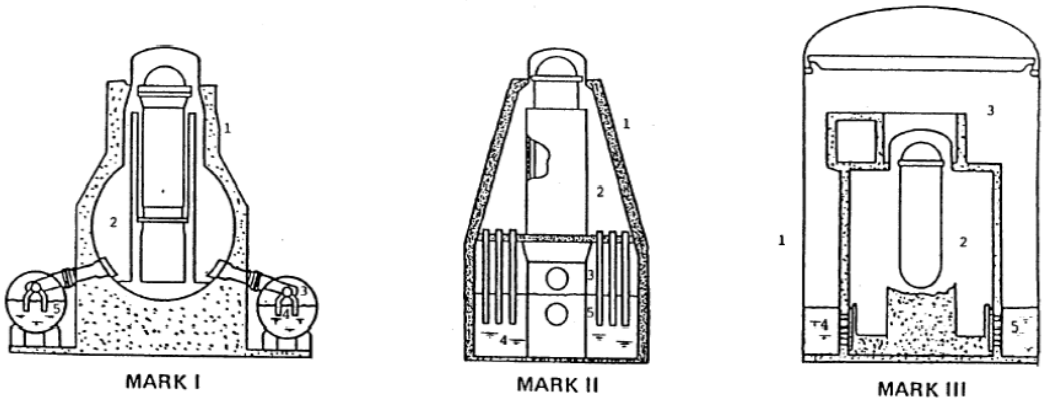

Figure 1. BWR pressure suppression system designs (NUREG-2196, 2016): 1-Primary containment, 2-Drywell, 3-Wetwell, 4-Suppression pool, 5-Vent system

NUREG-2196 (2016) report represents that how fluid comes into the suppression pool over time after LOCA occurs. Initially, a water in the downcomer is vented until about 0.3

seconds after a LOCA, and then a mixture of a non-condensable gas (NCG) and steam is pushed into a suppression chamber until around 20 seconds. After a flow level of the NCG is low from 20 seconds, the fluid entering the suppression pool becomes a steam-water mixture, and, in the suppression pool, the steam-water direct contact condensation occurs dominantly. Therefore, understanding of the heat transfer mechanism in steam-water direct contact condensation is essential since the direct contact condensation is the actual phenomenon that happens in BWRs suppression pool when a LOCA occurs.

Because of this importance, numerous studies have been performed on direct contact condensation. Especially, researches regarding the heat transfer coefficient have been actively conducted in order to understand the heat transfer characteristics at the interface between the steam and water. Brucker and Sparrow (1977) performed the steam bubble experiments of the direct contact condensation at six different pressures changing the pool temperature. The bubble collapse pattern was photographed using a high-speed camera, and the change of bubble volume at each steam pressure was analyzed. Based on these data, the condensation heat transfer coefficient was proposed. Fukuda (1981) experimented with the boundary conditions of varying nozzle diameter, steam mass flux, and pool temperature. Though the image analysis, the estimated heat transfer coefficient and the frequency were analyzed. Aya and Nariai (1991) proposed a regime map of the steam condensation in pool water at the low mass flux region of 0-40 $kg/m^2 \cdot s$ or less using the downward injection nozzle. In addition, the heat transfer coefficient was derived from two experiments (the bubble injection into the water and the water injection into the steam flow) and compared with previous studies. Kar *et al*. (2007) mathematically calculated the heat transfer coefficient using the different five equations and compared it with the experimental data of the previous researches.

In the stable condensation region, which is at the high mass flux region, the heat transfer coefficient is derived through a steam jet modeling unlike the methods that derive the heat transfer coefficient directly by measuring the required properties as mentioned above. Chun *et al*. (1996) proposed a condensation map of high steam mass flux region (≥200 kg/m^2·s). Through the steam condensation experiments conducted on vertical and horizontal nozzle changing the nozzle diameter and the pool temperature, the heat transfer coefficient was evaluated. Song *et al*. (1998) also conducted the experiments of the direct contact condensation with five different horizontal nozzles with various pool temperature at the high steam mass flux region (≥250 kg/m^2·s). Three steam jet shapes (conical, ellipsoidal, and divergent shapes) were proposed in his study, and a steam jet length and axial & radial temperature distributions were analyzed for each jet shapes. Kim *et al*. (2004) proposed the empirical correlation of the heat transfer coefficient using three models, interfacial transport due to turbulence intensity, interfacial transport due to surface renewal, and interfacial transport due to shear stress. They concluded that the temperature of the subcooled water does not significantly affect the heat transfer coefficient at the high steam mass flux region (≥300 kg/m^2·s). Wu *et al*. (2007) conducted the experiments of the direct contact condensation using with the convergent and divergent nozzle at the high steam mass flux region (≥298 kg/m^2·s). The maximum expansion ratio of the steam plume and the penetration length of the steam plume were derived, and then the correlation of the condensation heat transfer coefficient was proposed using the expansion ratio. Song *et al*. (2012) conducted experiments about the overall steam jet behavior in order to design the steam sparger contained in an IRWST pool in the APR 1400 reactor. The experimental data were also analyzed using computational fluid dynamics (CFD). The summary of the previous equations for the heat transfer coefficient is given in Table 1.

Table 1. Summary of proposed equations for the heat transfer coefficient from literatures

Authors	Instruments	G (kg/m^2 s)	d (mm)	T_f (°C)	Equation	h_H (MW/ m^2·K)
Brucker and Sparrow (1977)	High-speed camera	1.03-6.21 MPa	3	15-100	$h = \frac{\rho_v \left(\frac{dV}{dt}\right) h_{fg}}{A(T_{sat} - T_\infty)}$	0.01
Fukuda (1981)	High-speed camera Thermocouple	63-233	16.1	10-90	$\bar{h} = 43.78 \frac{\lambda_L}{d} \left(\frac{dG_s}{\rho_L \nu_L}\right)^{0.9} \frac{c_{PL}\Delta T}{h_{fg}}$	0.01-0.7
Simpson and Chan (1982)	High-speed camera Thermocouple	147-333	6.35-22.2	25-65	$h = \frac{\dot{m} h_{fg} A_0}{\Delta T A_c}$	0.15-0.69
Jeje *et al*. (1989)	High-speed camera Thermocouple	80-200	5	15-20	$\bar{h}(t) = \frac{\Lambda \Delta H_v}{A(t)(T_{sat} - T_b)}$	0.2-2.4
Aya and Nariai (1991)		0-40	18.29	10-85	$h = q \cdot (T_s - T_t)$	0.1-2.0
Chun *et al*. (1996)	High-speed camera Thermocouple	250-600	1.35-10.85	13-82	$h = 1.3583 \cdot c_p G_m B^{0.0405} \left(\frac{G}{G_m}\right)^{0.3714}$	1.0-3.5
Song *et al*. (1998)	High-speed camera Thermocouple	250-1240	5-20	20-95	$h = 1.4453 \cdot c_p G_m B^{0.03587} \left(\frac{G}{G_m}\right)^{0.13315}$	1.24-2.05
Kar *et al*. (2007)	High-speed camera Thermocouple	72	0.6-1	15-65	$h = \frac{v_c \Delta H_{lv} \rho_{v,l}}{T_v - T_c}$	0.9-6.5
Wu *et al*. (2007)	High-speed camera Thermocouple	298-723	2.2 and 3.0	19.8-69.8	$h_{con} = 0.1503 \sqrt{\frac{k_l c_p}{\nu_l \rho_v} \frac{1}{4 - 2\delta}} \cdot G_e^{0.75} \cdot G_m^{0.25} B^{0.3} \left(\frac{p_a}{p_s}\right)^{0.1}$	0.63-3.44
Gulawani *et al*. (2009)	Hot film anemometry Thermocouple	472-501	1-2	35-45	$h = \frac{l^2 R_w}{A_{film}(T_R - T_B)}$	0.1-4.0
Song *et al*. (2012)	High-speed camera Thermocouple	150-1250	5-20	20-90	$h = 1.445 \cdot c_p G_m B^{0.36} \left(\frac{G_0}{G_m}\right)^{0.1333}$	1.24-2.05

Compared with previous researches, there are two significances in this study. The first is to derive the heat transfer coefficient through experiments of the steam-water direct contact condensation in the unstable condensation region, which is at the steam mass flux of 5-65 kg/m^2-s. Although Aya and Nariai (1991) suggested the heat transfer coefficient correlation at low mass flux (0-40 kg/m^2-s), which is the chugging and condensation oscillation region, the calculated the heat transfer coefficient values are only represented without explaining about detailed experimental data and measurement techniques.

Except Aya and Nariai (1991), most of the previous works have been focused on the stable condensation region, which is the intermediate to high steam mass flux region, due to its high possibility of mechanical damage as Song *et al*. (2012) stated in their paper. However, the steam-water direct contact condensation in BWRs suppression chamber starts approximately 20 seconds following the LOCA. Initially the stable condensation occurs due to the high steam mass flux, but will change into the unstable condensation, which is a condensation oscillation (CO). This is because the temperature of the suppression pool increases due to entering the initial high steam flux, and the steam mass flux gradually decreases with time.

Therefore, since the unstable condensation is the actual phenomenon occurring in BWRs suppression pool, current study of the heat transfer characteristics in the low mass flux region would contribute to a better understanding of steam-water condensation process in nuclear reactor. Figure 2 shows the condensation regime of present experiments conducted at low steam mass flux of 5-65 kg/m^2-s with the pool temperatures of 70-95°C.

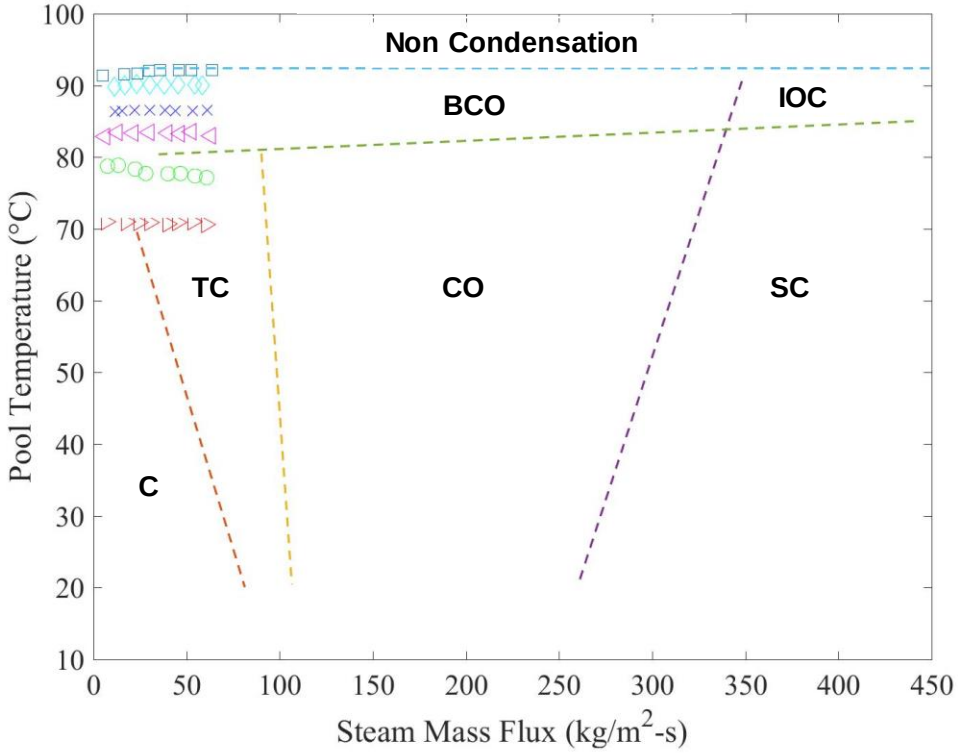

Chugging (C), Transitional Chugging (TC), Condensation Oscillation (CO), Bubbling Condensation Oscillation (BCO), Stable Condensation (SC), and Interfacial Oscillation Condensation (IOC).

Figure 2. Condensation regime map of the present experiments

Second, several previous researches have been used thermocouples to measure the pool temperature. The measurement method using thermocouples inherently have drawbacks such as point wise, intrusive, and low sampling rate measurement. So, a change of an average bulk temperature might be presented, but it is difficult to measure an instantaneous local temperature change. In order to overcome the disadvantages, the general pattern of the steam flow in the suppression pool was developed, and then a local pool temperature was derived based on the average bulk temperature measured by thermocouples under the assumption that the steam flows

as the developed pattern in most situations in NUREG-0783 (1981) report. The local temperature, however, is derived based on the assumption, not the local temperature measured by actual experiments. Gulawani *et al*. (2009) measured the local pool temperature using Constant temperature anemometry (CTA) and Hot film anemometry (HFA), and compared the measured local temperature with the predicted temperature from CFD. But the HFA and CFA can only measure the local temperature of the pool, not the temperature field of the pool unlike the LIF method. Thus, in this study, both thermocouples and LIF method have been utilized to measure not only the average temperature in the pool but also the temperature field of the pool to show accurately the instantaneous temperature change occurring at the interface between the water and the steam where the heat transfer occurs.

In summary, the goal of this study is to conduct the experiments of the steam-water direct contact condensation and to investigate on the heat transfer characteristics like the heat transfer coefficient at the low mass flow region (5-65 kg/m^2-s) where an unstable condensation occurs. Also, the temperature distribution in the pool is measured by LIF and thermocouples, and the bubble equivalent diameter in the unstable condensation is analyzed by an image processing technique.

2. METHODOLOGY

The fundamental concept of the heat transfer coefficient correlation is based on Newton's law of cooling as:

$$q'' = \frac{q}{A} = h_H \cdot \left(T_s - T_f\right) \tag{1}$$

where q'' is the heat flux in W/m^2, q is the heat transfer rate between the steam and the pool in W, A is the surface area of the steam bubble in m^2, h_H is the convective heat transfer coefficient in W/m^2·K, T_s is the temperature of the steam in Kevin, and T_f is the temperature of the pool in Kevin.

q can be also described as:

$$q = \dot{m} \cdot c_p \left(T_s - T_f\right) \tag{2}$$

where $\dot{m}$ is the flow rate of the steam in kg/s and c_p is the specific heat of the steam in J/kg·K.

Therefore, the heat transfer coefficient can be calculated as following:

$$h_H = \frac{\dot{V} \cdot \rho \cdot (h_s - h_f)}{A \cdot \left(T_s - T_f\right)} \tag{3}$$

where $\dot{V}$ is the condensed volumetric flow rate of the steam in m^3/s, ρ is the density of the steam in kg/m^3, h_s is the enthalpy of the steam at the given temperature and pressure in kJ/kg, and h_f is the enthalpy of the water at the pool temperature in kJ/kg.

Eq. (3) is the equation of Brucker and Sparrow (1977) is adopted for this study to calculate the heat transfer coefficient since most variables in this correlation can be obtained

through LIF, thermocouples, and image processing technique that are the main methods of this study.

$\dot{V}$ is the condensed volumetric flow rate calculated by Eq. (4).

$$\dot{V} = \dot{V}_{\text{exp}} - \dot{V}_{\text{cal}} \tag{4}$$

where $\dot{V}_{\text{exp}}$ is the expected volume flow rate, which is the measured volumetric flow rate of the steam at the inlet region and $\dot{V}_{\text{cal}}$ is the calculated volume flow rate of the steam after condensation.

For a deeper understanding of the steam condensation, bubble's equivalent diameter of the wetted surface where the mass transfer occur can be calculated as follows:

$$D_{b,eq} = \sqrt{\frac{4A_b}{\pi}} \tag{5}$$

where A_b is the wetted surface area of the bubble at a given time.

In this study, T_f is measured using both LIF and thermocouples, $\dot{V}_{\text{cal}}$ and A are measured using high-speed camera imaging techniques. The other properties, T_s, h_s, h_f, ρ and $\dot{V}_{\text{exp}}$ are measured and evaluated by the DAQ data.

2.1 Image Processing

The condensation visualization method consists of two steps, obtaining high definition pictures of the steam bubble at high frame rates and bubble tracking using image processing.

Figure 3. shows the LED backlight setup to obtain high quality images.

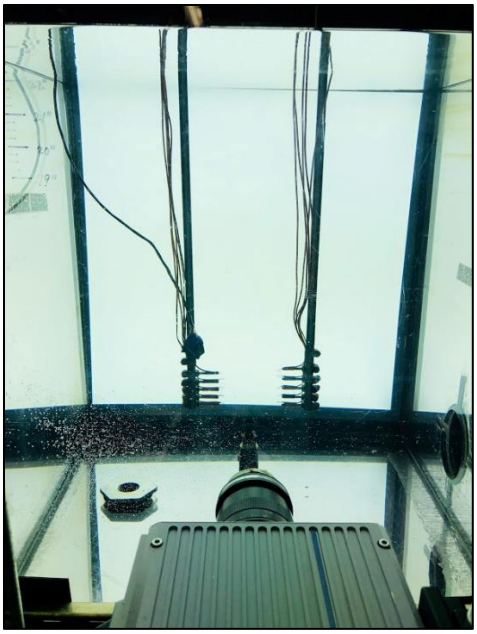

Figure 3. LED backlight setup

The backlight located behind the pool is acting as a source of shadowgraph as well as a constant light intensity enhancement to reduce undesired noise of the raw image captured from the sensor of a high-speed camera. More details about each instrument will be explained in the experimental setup section.

The images captured from the high-speed camera are pre-processed to obtain the physical characteristics of the bubble as shown in Figure 4 (a). Using a commercial program, Image J, binary images can be obtained in order to gain the information of the interface between the bubble and the subcooled water as shown in Figure 4 (b). A bubble tracking program is developed to extract surface area, volume, cross-sectional area, and the equivalent diameter of steam bubbles from the consecutive high-speed images using the image processing program. The program automatically detects the irrelevant objects other than the traced bubbles such as the

thermocouples and the jet nozzle and eliminates from the image plane to prevent further interference of extracting the useful bubble information as shown in Figure 4 (c).

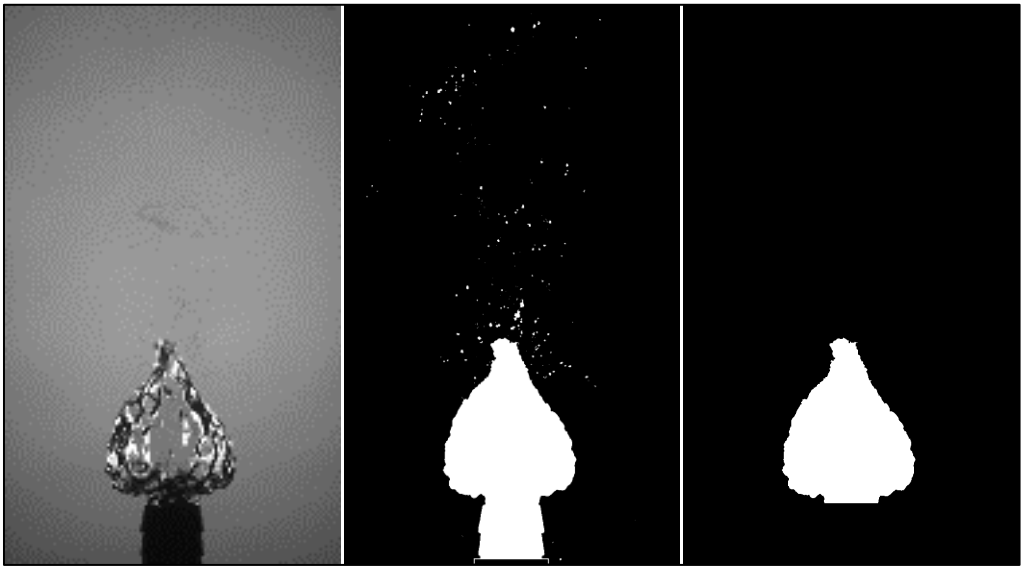

(a) **Raw image** **(b) Binary image** **(c) Processed image**

Figure 4. Example photographs of image processing (T_f **: 70 °C,** G **: 6.95 kg/m^2-s)**

The volume and surface area of the bubbles are calculated by assuming the azimuthal symmetry, and numerical integration using cylindrical geometry. The height of the cylinder is 1 pixel, while the diameter is the number of pixels found in that lateral-wise axis. The integration of all the volumes and surface areas of the cylinders can calculate the total volume and surface area of the bubble.

2.2 Laser-Induced Fluorescence (LIF)

LIF is used to measure the pool temperature, which changes in a short period of time at the moment of condensation. LIF is one of the methods to visualize the temperature field by using the fluorescence phenomena of a dye occurred by the laser. The fluorescence emission intensity can be defined as:

$$I = I_0 C \phi \varepsilon \tag{6}$$

where I_0 is the incident laser beam intensity in W/m^2, C is the concentration of the dye in kg/m^3, ϕ is the fluorescence quantum efficiency, and ε is the absorption coefficient in m^3/kg.

In this study, Rhodamine B (Rh B) has been used for the fluorescent dye since its temperature sensitivity is large (2.3%/K) compared to other organic dyes. Rh B concentration was 20 mL of 1g/L Rh B aqueous solution with 1 mL of Isopropyl alcohol in 191 ± 1.72 L of water.

Figure 5 shows an example of the calibration between the pool temperature and the light intensity proposed by Yang *et al*. (2019). Figure 5 (a) represents the fluorescence spectra of the Rh B measured by a spectrometer, and Figure 5 (b) shows the exponential curve fitting used to calculate the correlation between the pool temperature and the intensity of the light.

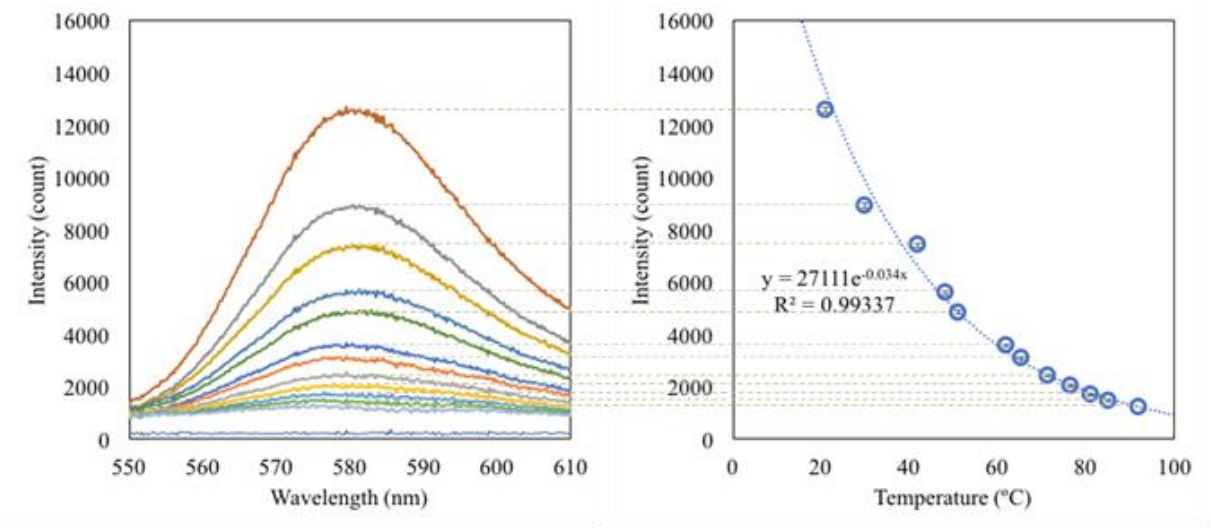

(a) Fluorescence spectra of Rhodamine B measured by spectrometer

(b) Exponential curve fitting

Figure 5. Example of calibration between pool temperature and light intensity

The fluorescence spectra of Rh B has a characteristic, which is that the intensity of emitted light for 584 nm wavelength has a proportionality to temperature as shown in Figure 5 (a). The intensity difference by the temperature is clearly distinguished around 580 mm peak. In additions, the intensity decreases as the temperature increases and especially at the low temperature dramatically decreases compared to the high temperature region. So, an exponential curve fitting is suitable to calibrate the correlation between the pool temperature and the intensity of the fluorescence of Rh B as shown in Figure 5 (b).

Based on the relationship between the pool temperature and the light intensity, total 6,000 photographs (1,000 images per one calibration temperature) are recorded without the steam for 6 calibration temperatures with the temperature range of 70 to 95 °C (at intervals of 5 °C) using a high-speed camera with the full resolution of 1,280x860 and frame rate of 1,000 fps in order to calibrate LIF data of current study. After time averaging the 1,000 photos per each calibration

temperature, total 6 time-averaged images are generated and accumulated into one integrated image. The integrated image is divided by 4x4 pixel and has a total of 68,800 windows. In a single window, 12 pieces of temperature information are accumulated. According to camera sensor-specific calibration proposed by Yang *et al.* (2019), the averaged intensity of calibration curve of 68,800 decreases steadily as the temperature increase like Figure 5's result.

The camera sensor detects a certain number of photons regardless of the intensity of the photons. Since the 580 nm bandpass filter is used, the camera sensor can capture images with 580±20 nm wavelength regardless of photon intensity. As shown in Figure 5, when the intensity is high (pool temperature is low), the difference between the peak value and the surrounding value is distinguished clearly, which means that high resolution could be obtained when normalized. So, it can be reported that the distribution of the intensity is smaller when the pool temperature is low while the distribution of the intensity increases as the temperature increases.

Figure 6 presents the three main instruments required to conduct LIF experiments; a 532 nm continuous laser, a LED backlight as a diffusive optical source, and a high-speed camera with 580 bandpass filter.

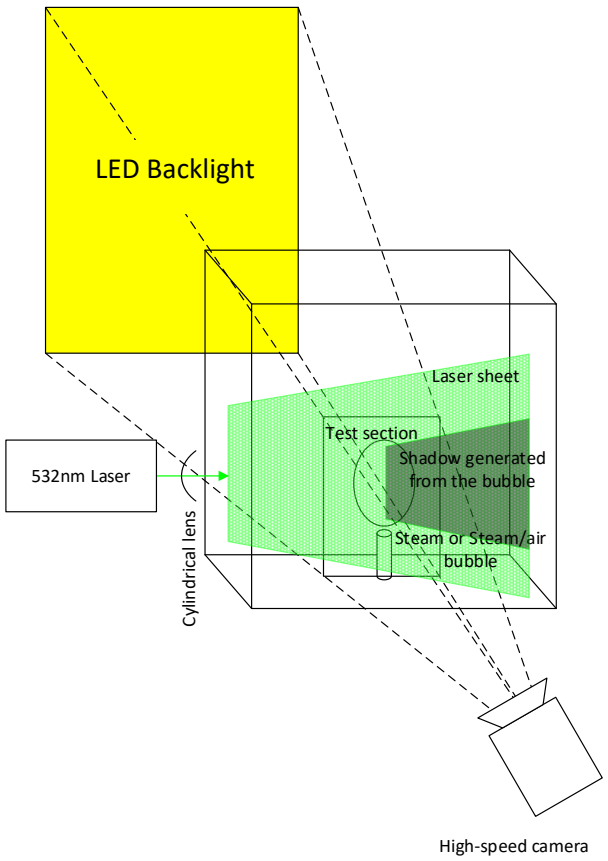

Figure 6. Schematic of LIF setup

Using this LIF setup, the experiments of the steam-water direct contact condensation are performed for various steam flow rate. Figure 7 shows the example images (raw and calibrated images) at a temperature of 75 °C and the mass flow rate of 0.5 g/s.

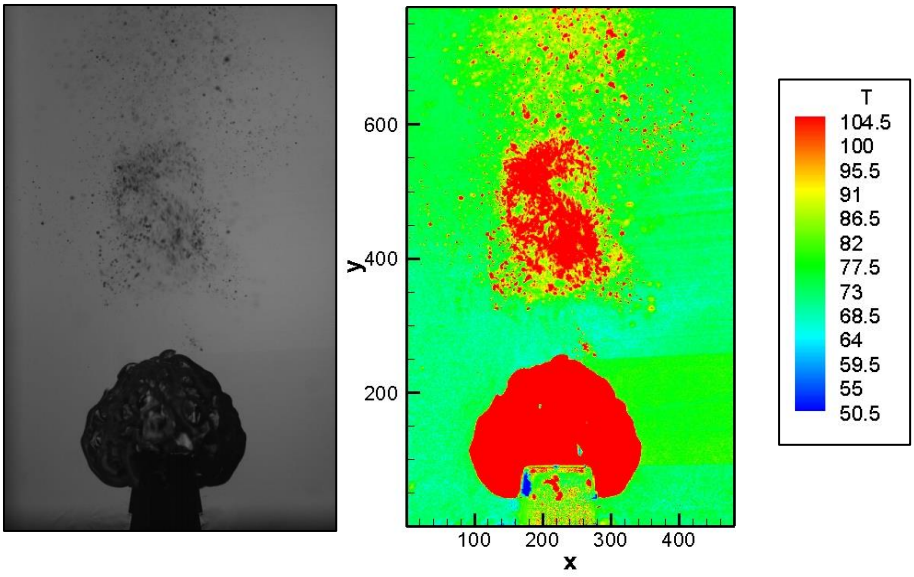

Figure 7. Example images using LIF (Left: raw image, right: calibrated image)

Based on the calibration data as shown in Figure 7, the temperature distribution of the pool will be analyzed in the results and discussion section.

3. EXPERIMENT

3.1 Experimental Setup

The experimental facility has been designed to investigate the heat transfer coefficient in steam-water direct contact condensation using LIF as shown in Figure 8 and 9.

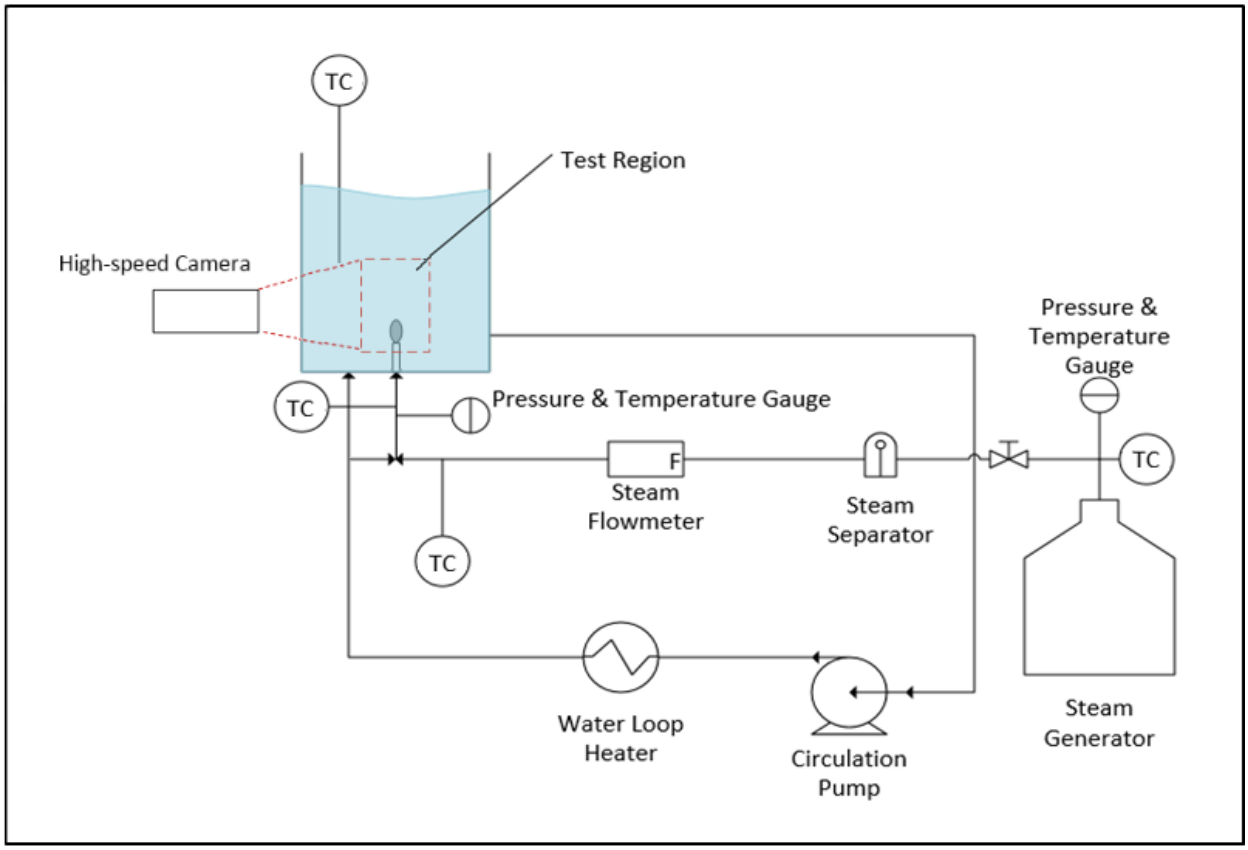

Figure 8. Schematic diagram of experimental facility

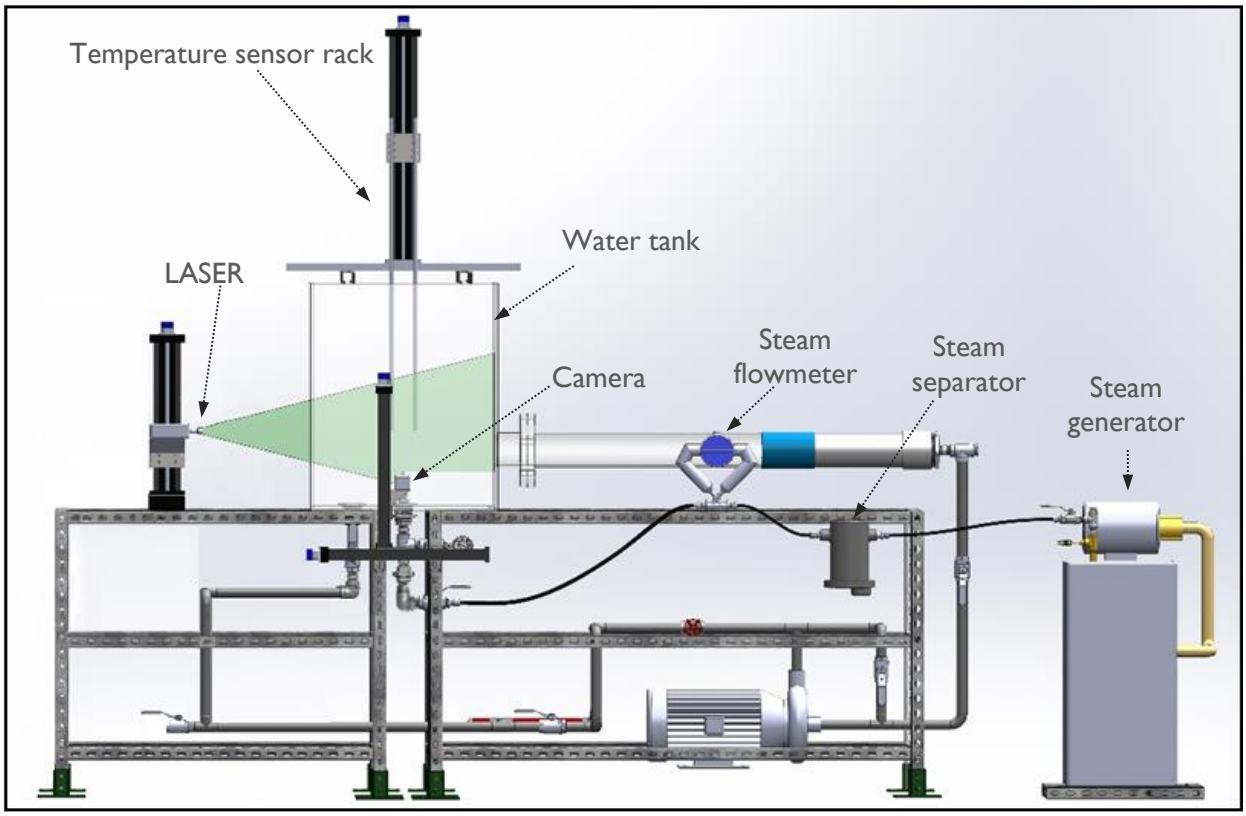

Figure 9. Drawing of the experimental facility

This facility consists of three major components, which are a steam supply section, a test section, and data measurement system. The steam supply system produces and controls the steam flow and temperature. The steam produced from the steam generator is injected into the sub-cooled water tank, and then the bubbles of the steam will be condensed during phase change. The test section with the laser and high-speed camera is used to capture the image of the condensing bubbles. To measure the temperature, both K-type thermocouples and LIF method are used. The pressure of the steam is measured by pressure transducers. All measured data is collected in DAQ and then transferred into a computer to analyze the data.

3.1.1 Steam Supply Section

The overall design of the steam supply section is presented in Figure 10, and an isometric view of the steam supply system is shown in Figure 11.

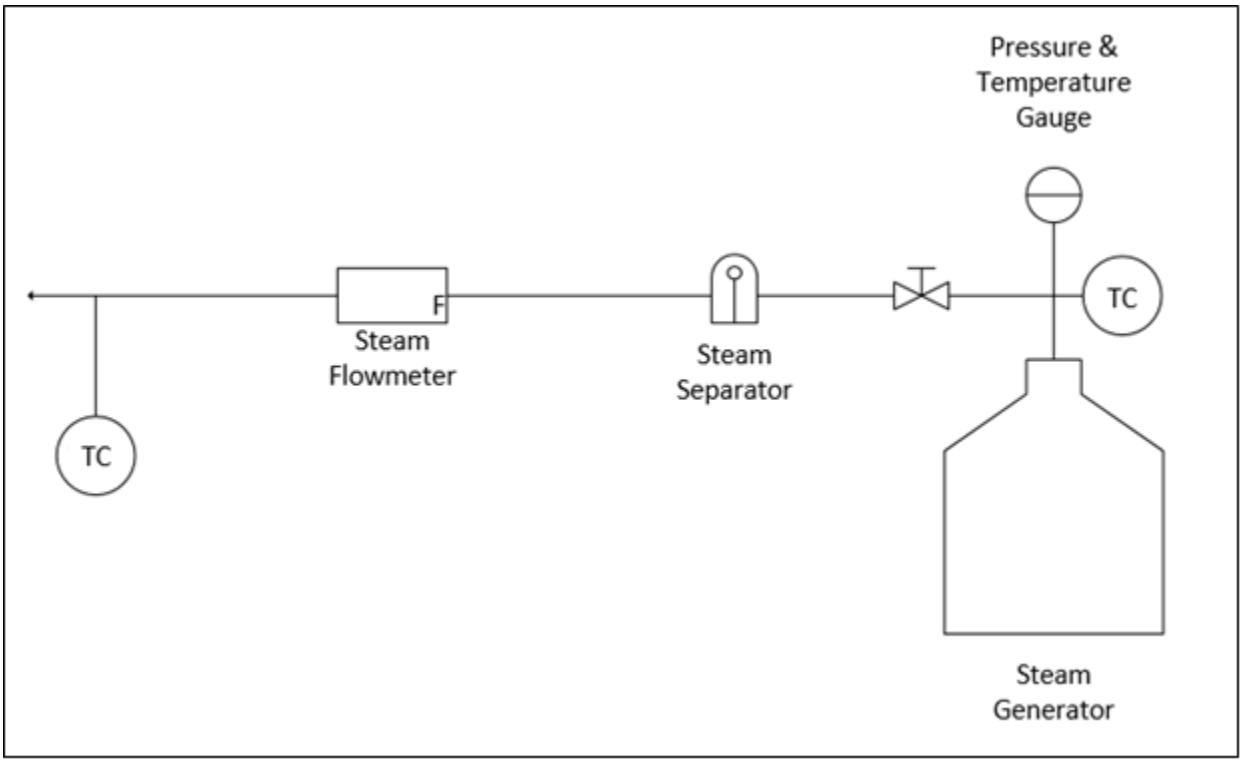

Figure 10. Schematic diagram of experimental facility

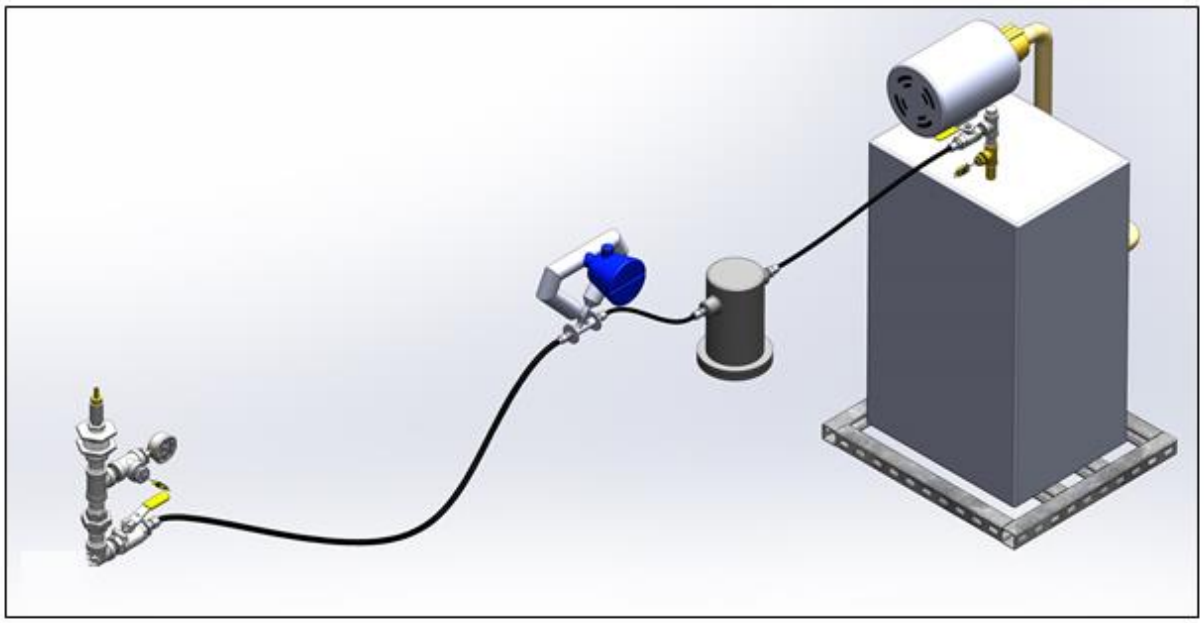

Figure 11. Isometric view of steam supply system

The steam is produced in the Sussman Electric Boiler Model ES-18 as shown in Figure 12, which provides a maximum steam rate of 6.829 g/s and has a design pressure 0-689.4 kPa. The control valve located on the steam outlet adjusts the steam mass flow rate. The steam supply line is insulated by fiberglass covering to maintain the saturated steam.

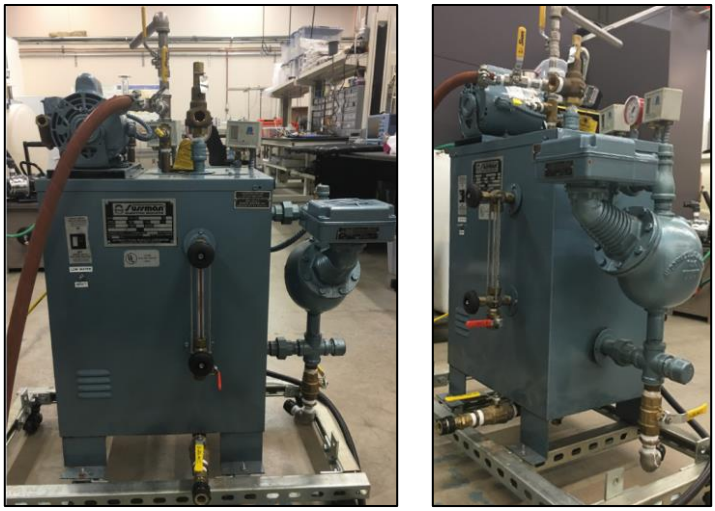

Figure 12. Steam generator

In order to remove water droplets, the steam travels through a steam separator model 81SATO designed for a maximum temperature of 111.2 °C, and a maximum pressure of 1,034.2 kPa as shown in Figure 13. The temperature and flow rate of the steam are measured by a K-type thermocouple and a flowmeter, Micro Motion Coriolis flowmeter model CMF025 as shown in Figure 14, which has flow accuracy with gases of ± 0.75% of rate. Band type heaters are wrapped around the steam pipeline located below the water tank to maintain high-quality saturated steam. To measure the temperature of the steam, the K-type thermocouple is installed right before entering the test section, where is below the water tank.

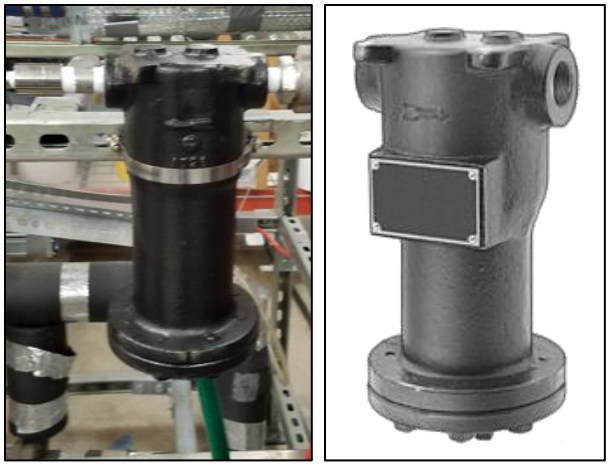

Figure 13. Steam separator

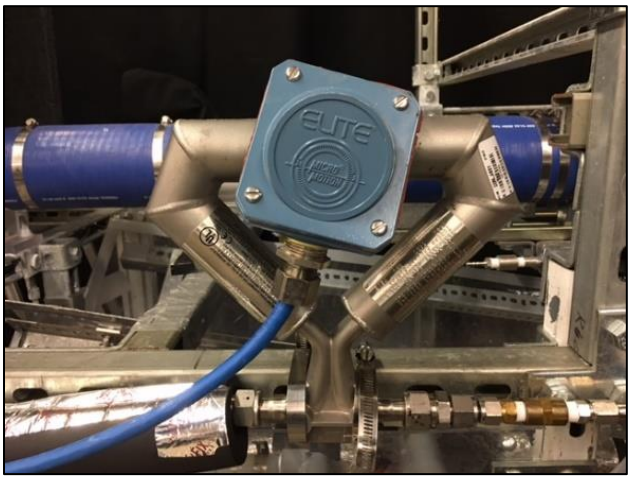

Figure 14. Coriolis flow meter

3.1.2 Test Section

The whole test section is in a water tank with dimensions of 609.6 mm x 609.6 mm x 774.7 mm (24 in. x 24 in. x 30.5 in.) in width x depth x height as shown in Figure 15. The detailed dimensions of the test section are provided in Figure 16. The nozzle at the center of the water tank is 9.525 mm inner diameter and located at 42 cm ± 1 cm below the free surface of the water pool.

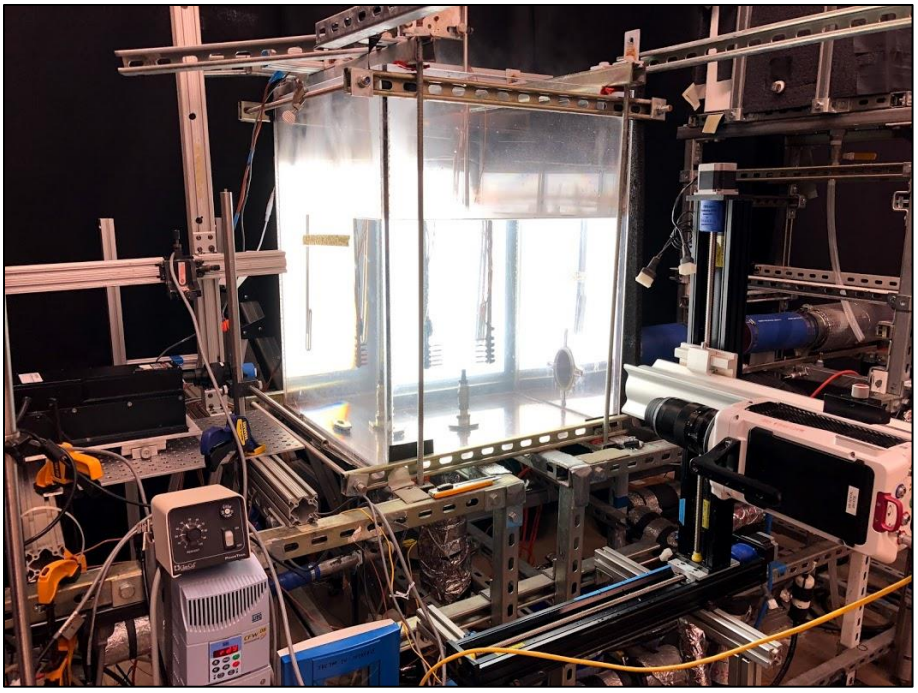

Figure 15. Photographic of the test section

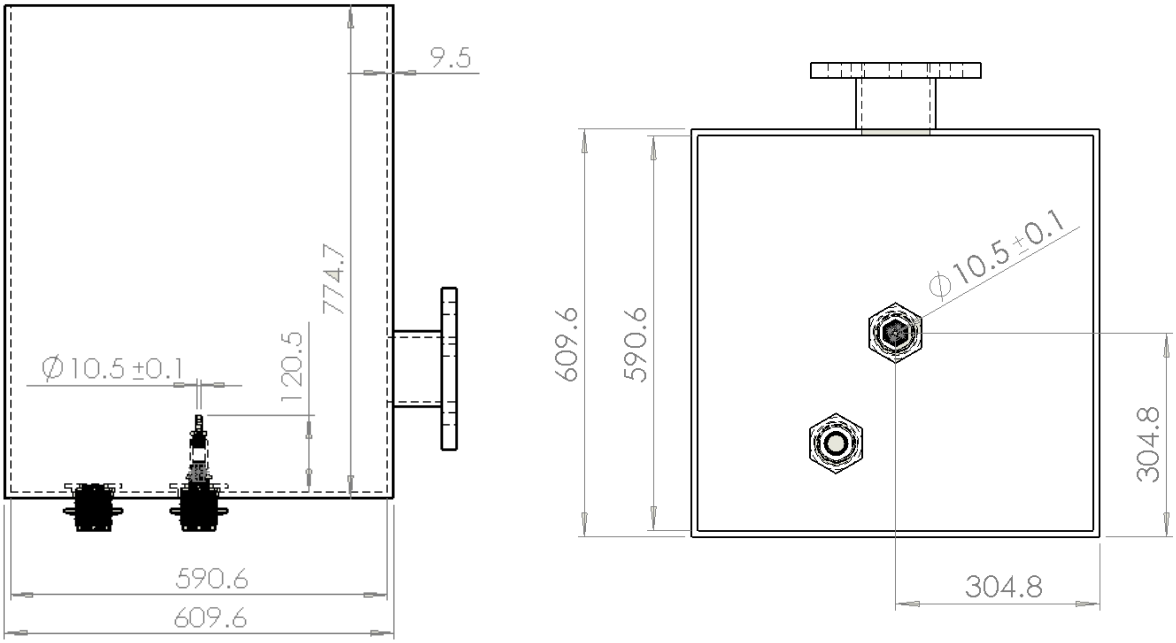

Figure 16. Test section 2D drawings: Front view (Left), Top view (Right)

Ten K-type thermocouples are located near the nozzle to measure the temperature of the water as shown in Figure 17. They are arranged in groups of 5 at opposite directions of the nozzle and held by a traverse system that is capable of adjusting their location in the z-direction. To achieve a desired water tank temperature, the water is circulated and heated up before injecting steam.

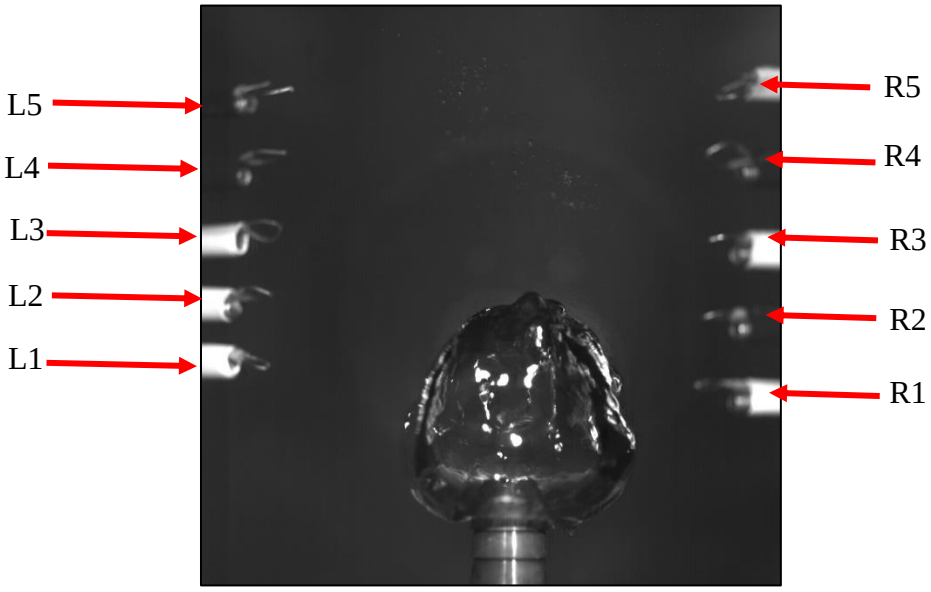

Figure 17. Thermocouples labeling

Figure 18 shows the components of the test section such as a high-speed camera, a continuous laser, and a LED backlight. The description and specific models are described in Table 2.

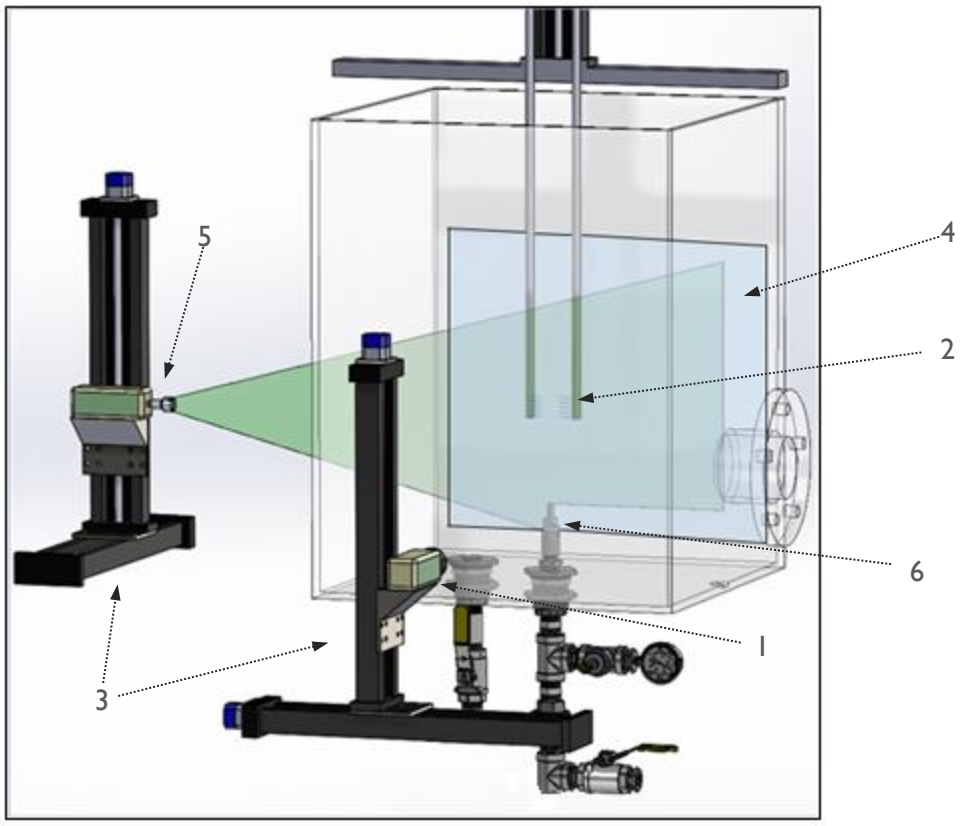

Figure 18. Configuration of the test section

Table 2. Description of test section components

Label	Description	Model
1	High-speed camera	Phantom V711
2	Thermocouples	K-Type
3	1-D Traverse	VXM step motor
4	LED Backlight	PBD-6060
5	10 W Laser	LSR 532W
6	Jet Nozzle	9.525 mm inner diameter

Figure 19 shows the laser system used in current experiments for continuous lasing.

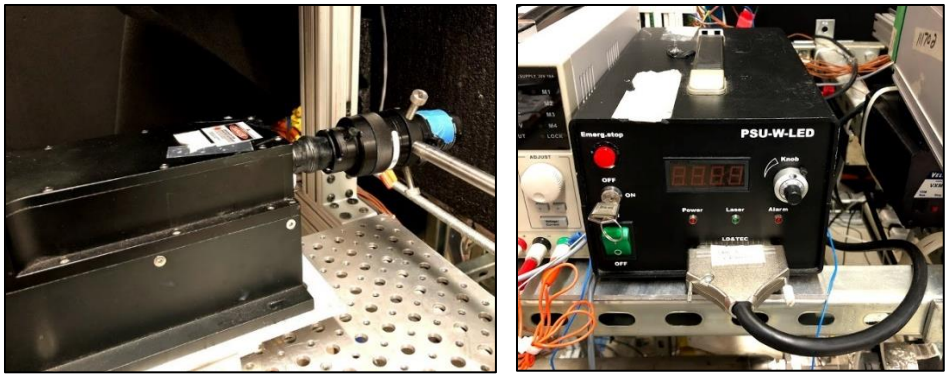

Figure 19. 10 W laser system

The 10W laser model LSR 532W is equipped on the experimental facility for LIF. The laser is designed for a wavelength of 532.515 nm and power stability of 5%. It can provide an enough intensity beam is able to be adjusted from having an operation to a desired frequency.

In order to capture the bubble images, a LED backlight is installed behind the water. The LED backlight model PBD-6060 is utilized to make a shadow graphic effect as shown in Figure 20. This white LED has 600 x 600 (L x W). Also, it has visible light quantity of 4,100 lumens, and power consumption of 48 W.

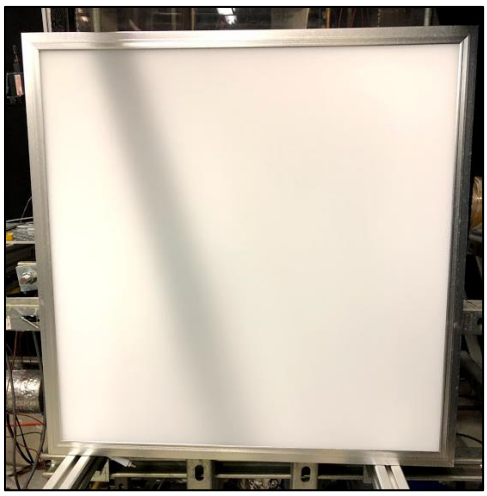

Figure 20. LED backlight (PBD-6060)

A high-speed camera installed in front of the pool is the Phantom v711 as shown in Figure 21. It has 1280 x 800-pixel resolution with 7,530 frames per second and a maximum frame rate of 680,000 fps at 128 x 80 pixel. Also, the 580 nm bandpass filter is installed at the front of the lens in order to filter wavelengths outside the 580 ± 20 nm. The traverse can be moved in two different locations to adjust the camera location for the desired picture frame.

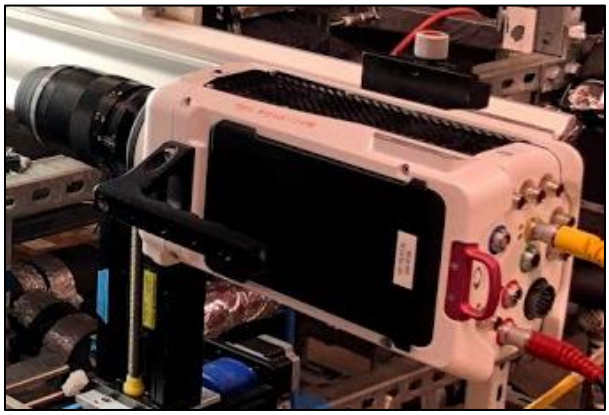

Figure 21. High-speed camera (Phantom V711)

3.1.3 Data Measurement System

At the experimental facility, high-quality system is equipped to measure accurate properties. The temperature of fluids is measured by using K-type thermocouples, which have an accuracy of 1 °C and a range of 0-1250 °C. In order to measure the pressure of the fluid, the pressure transducers, which have a range of 0-50.0 psi and ± 0.02 % FSO (Full-Scale Output)/g accuracy, are used. Each measuring instrument is connected to a Data Acquisition (DAQ), model NI SCXI-1000 made by National Instruments as shown in Figure 22. All data transferred via DAQ Assistant are integrated by using the LabVIEW program. The sampling rate and time for each experiment are 1.0 kHz and 30 s.

Figure 22. DAQ (NI SCXI-1000)

3.2 Experimental Procedure

The experimental procedure not only includes the preparation for the main components such as the water tank, the steam generator, and the data acquisition system but also the actual experimental flow.

At first, the water tank is filled with purified DI water and heated until to desired pool temperature using water heaters. During using the water heaters, the circulation pump must be turned on to prevent the water heater from overheating. Total 20 mL of Rhodamine-B is resolved into the water tank (212 liters of DI water) and mixed for LIF. While heating, LIF images are taken for calibration without steam from room temperature 20°C to target temperature 70 - 95°C with intervals of 5-10°C.

The steam generator is connected to DI water system to fill the DI water for making the steam. The steam generator is turned on and connected to the steam separator that rust removal

was completed before the experiments. Prior to actual experiments, the steam must be injected sufficiently to extract all air in the tube. The camera is adjusted at the top of the nozzle to capture the maximum volume of the bubble and set to take 1,000 sheets per second.

DAQ preparation ensures that data acquisition systems are functioning correctly before the test is started. First, open and run LabVIEW Vi required for the test to observe and check the values of the instruments. If they don't match the following values in Table 3, the instruments should be corrected. After the preparations are completed, the test is ready to be initiated. Also, all the experimental conditions are summarized in Table 4.

Table 3. Target values

Instrument	Value
Thermocouple	70 - 95 °C
Coriolis Flowmeter	~ 0 g/s
Pressure Transducer	~ 14.7 psia

Table 4. Experimental conditions

Parameter	Value	Unit
Steam temperature (T_s)	> 101	°C
Pressure in pool (P)	~ 110	kPa
Steam flow rate ($\dot{m}$)	0.36-4.55	g/s
Steam mass flux (G)	5.05-64.85	kg/m^2-s
Pool temperature (T_f)	71/78/83/86/90/92	°C

Total 48 experiments are performed at pool temperatures of 70 to 95°C $\pm$ 1°C, with different steam mass fluxes between 5 and 65 kg/m^2-s. The test matrix is shown in Table 5 including averaged flow properties measured by experimental apparatuses.

Table 5. Test matrix (averaged properties after measurement)

Test #	T_f (°C)	T_s (°C)	$\dot{m}$ (g/s)	G (kg/m^2-s)	h_f (kJ/kg)	h_s (kJ/kg)	ρ_s (kg/m^3)
S1-1	71.00	100.97	0.50	6.95	297.21	2677.09	0.62
S1-2	70.96	101.04	1.26	17.72	297.06	2677.20	0.62
S1-3	70.94	101.24	1.73	24.22	296.97	2677.52	0.62
S1-4	70.91	101.49	2.16	30.26	296.83	2677.92	0.63
S1-5	70.74	101.88	2.85	40.05	296.11	2678.53	0.64
S1-6	70.93	102.06	3.22	45.13	296.91	2678.80	0.64
S1-7	71.06	102.39	3.79	53.23	297.45	2679.33	0.65
S1-8	70.66	102.74	4.32	60.56	295.77	2679.87	0.65
S2-1	78.75	102.10	0.54	7.58	329.71	2678.87	0.64
S2-2	78.87	102.79	0.95	13.36	330.20	2679.96	0.66
S2-3	78.35	102.12	1.59	22.38	328.02	2678.91	0.64
S2-4	77.74	101.53	2.00	28.13	325.45	2677.98	0.63
S2-5	77.68	101.59	2.85	40.00	325.23	2678.07	0.63
S2-6	77.74	101.29	3.33	46.77	325.45	2677.61	0.62
S2-7	77.38	101.63	3.89	54.52	323.95	2678.14	0.63
S2-8	77.15	102.21	4.34	60.84	323.00	2679.05	0.64
S3-1	82.86	100.93	0.44	6.20	346.94	2677.03	0.62
S3-2	83.42	101.61	0.92	12.86	349.33	2678.11	0.63
S3-3	83.33	101.64	1.51	21.21	348.91	2678.16	0.63
S3-4	83.44	102.09	2.12	29.82	349.40	2678.85	0.64
S3-5	83.38	101.95	2.83	39.69	349.14	2678.64	0.64
S3-6	83.26	101.90	3.31	46.41	348.64	2678.56	0.64
S3-7	83.59	102.26	3.74	52.44	350.02	2679.13	0.64
S3-8	83.02	102.51	4.48	62.91	347.61	2679.52	0.65

Table 5 Continued. Test matrix (averaged properties after measurement)

Test #	T_f (°C)	T_s (°C)	$\dot{m}$ (g/s)	G (kg/m^2-s)	h_f (kJ/kg)	h_s (kJ/kg)	ρ_s (kg/m^3)
S4-1	86.37	101.09	0.84	11.83	361.69	2677.29	0.62
S4-2	86.46	100.84	1.09	15.31	362.06	2676.90	0.62
S4-3	86.57	101.17	1.56	21.91	362.56	2677.42	0.62
S4-4	86.56	101.36	2.16	30.30	362.52	2677.71	0.63
S4-5	86.50	101.53	2.73	38.38	362.27	2677.98	0.63
S4-6	86.44	101.65	3.13	43.94	362.02	2678.17	0.63
S4-7	86.43	102.07	3.79	53.14	361.95	2678.83	0.64
S4-8	86.50	102.40	4.35	61.09	362.24	2679.34	0.65
S5-1	89.83	100.89	0.81	11.34	376.24	2676.97	0.62
S5-2	90.03	100.89	1.20	16.81	377.08	2676.98	0.62
S5-3	90.17	101.22	1.66	23.26	377.68	2677.50	0.62
S5-4	90.14	101.45	2.15	30.24	377.55	2677.86	0.63
S5-5	90.10	101.61	2.70	37.94	377.41	2678.10	0.63
S5-6	90.13	101.95	3.25	45.63	377.53	2678.63	0.64
S5-7	90.12	102.26	3.89	54.53	377.46	2679.12	0.64
S5-8	90.01	102.37	4.16	58.43	376.99	2679.30	0.65
S6-1	91.37	100.75	0.36	5.01	382.73	2676.75	0.61
S6-2	91.54	100.96	1.17	16.35	383.46	2677.08	0.62
S6-3	91.68	101.23	1.69	23.75	384.03	2677.52	0.62
S6-4	92.09	101.34	2.12	29.75	385.76	2677.68	0.63
S6-5	92.11	101.60	2.54	35.67	385.87	2678.09	0.63
S6-6	92.13	101.88	3.27	45.92	385.91	2678.53	0.64
S6-7	92.18	102.26	3.74	52.43	386.13	2679.12	0.64
S6-8	92.18	102.99	4.55	63.84	386.13	2680.26	0.66

The following steps are the actual test procedure to conduct a steam-water condensation experiment using LIF.

1. The water is heated up to the target temperature.
2. The heaters are disconnected from the power supply.
3. The circulation pump is turned off.
4. The LED backlight is turned on.
5. The steam generator valve is controlled to make the target flow rate using the HART screen of the Coriolis flowmeter.
6. The laser is turned on.
7. LabVIEW program is run and rechecked to verify all values transferred from the DAQ.
8. The images are recorded using the high-speed camera
9. The data acquisition is started using LabVIEW program.
10. Once the recording is finished, the data acquisition from LabVIEW is completed as well.
11. The laser is turned off.
12. The LED backlight is turned off.
13. The recorded image files are saved.

4. RESULTS AND DISCUSSION

Total 48 steam direct contact condensation experiments in subcooled water pool have been conducted. Through the analysis of the experimental data, the three results are discussed. First, the heat transfer coefficient, which is the core parameter of this study, is evaluated depending on time and steam mass flux variables and discussed how it correlates with previous studies. Second, experimental results of the pool temperature measured by thermocouples and LIF are compared, and the temperature distribution of the pool is visualized. Lastly, depending on time and steam mass flux variables, the changes in the bubble equivalent diameter are analyzed.

4.1 Heat Transfer Coefficient

As mentioned in the methodology section, the heat transfer coefficient can be calculated using the correlation proposed by Bruker and Sparrow (1997) in Eq (7).

$$h_H = \frac{\dot{V} \cdot \rho \cdot (h_s - h_f)}{A \cdot \left(T_s - T_f\right)} \tag{7}$$

The heat transfer coefficient has been evaluated through an image processing technique, based on DAQ measurement data. Figure 23 shows the evaluated heat transfer coefficient from the tests.

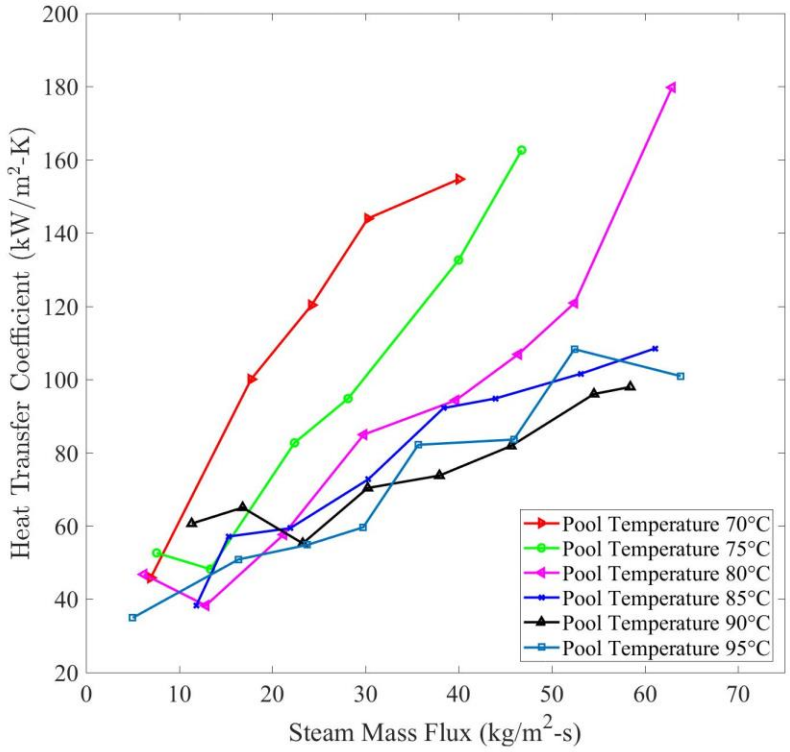

Figure 23. Heat transfer coefficient vs. Steam mass flux

The average heat transfer coefficient is found in range of 24.57-179.78 kW/m^2·K. Also, the averaged heat transfer coefficient for all tests is 87.66 kW/m^2·K. The averaged heat transfer coefficient increases as the steam mass flux increases, while the averaged heat transfer coefficient decreases as the pool temperature increases since the temperature difference between the steam and the water decreases.

Since the steam mass flux and the pool temperature are the boundary conditions of the current study, sensitivity analysis on these parameters is required to investigate the heat-transfer characteristics through comparison with previous research. Figure 24 presents the experimental results of the heat transfer coefficient of the current study including the research result suggested by Fukuda (1981).

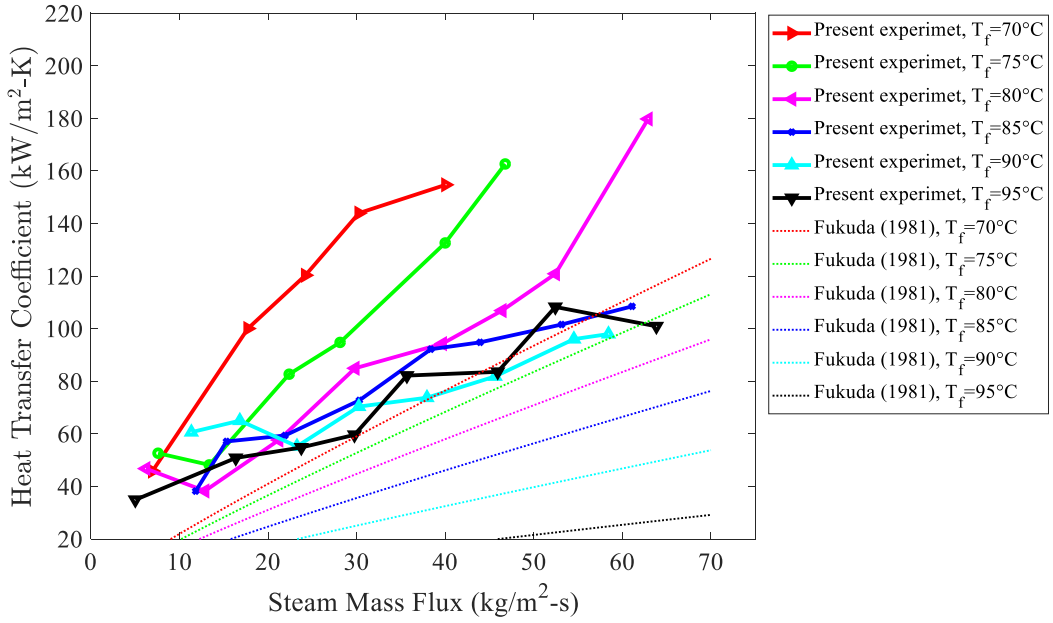

Figure 24. Heat transfer coefficient vs. Steam mass flux with Fukuda (1981)

The result of the heat transfer coefficient proposed by the Fukuda (1981) is plotted based on Eq. (8).

$$\bar{h} = 43.78 \frac{\lambda_L}{d} \left(\frac{dG_s}{\rho_L \nu_L} \right)^{0.9} \frac{c_{PL} \Delta T}{h_{fg}} \tag{8}$$

where λ_L is the thermal conductivity of the liquid in W/m·K, d is the nozzle diameter in mm, G_s is the steam mass flux in kg/m^2·s, ρ_L is the liquid density in kg/m^3, ν_L is the kinematic viscosity of the liquid in m^2/s, c_{PL} is the specific heat of the liquid in J/kg·K, ΔT is the temperature difference between the steam and the pool in K, and h_{fg} is the enthalpy difference between the steam and the pool in J/kg.

The results of Fukuda (1981) show that the value of the heat transfer coefficient tends to increase as the steam mass flux increases and to decrease as the temperature of the sub-cooled water increase, which is similar to the current study.

Both plots, however, do not match exactly. The reason can be estimated as follows. First, the correlation of Fukuda (1981) is based on the experimental data at the steam mass flux of 63-233 kg/m^2·s. Therefore, it might be different because it is projected and plotted in the current study's steam mass flux area, which is 0-65 kg/m^2·s. Another reason is that the nozzle orientation of the current study is vertically upward, while Fukuda (1981) is vertically downward, which may result in differences between both studies.

Figure 25 presents the experimental results of the current study and the correlations proposed by Song *et al*. (1998) and Chun *et al*. (1996) related to the heat transfer coefficient.

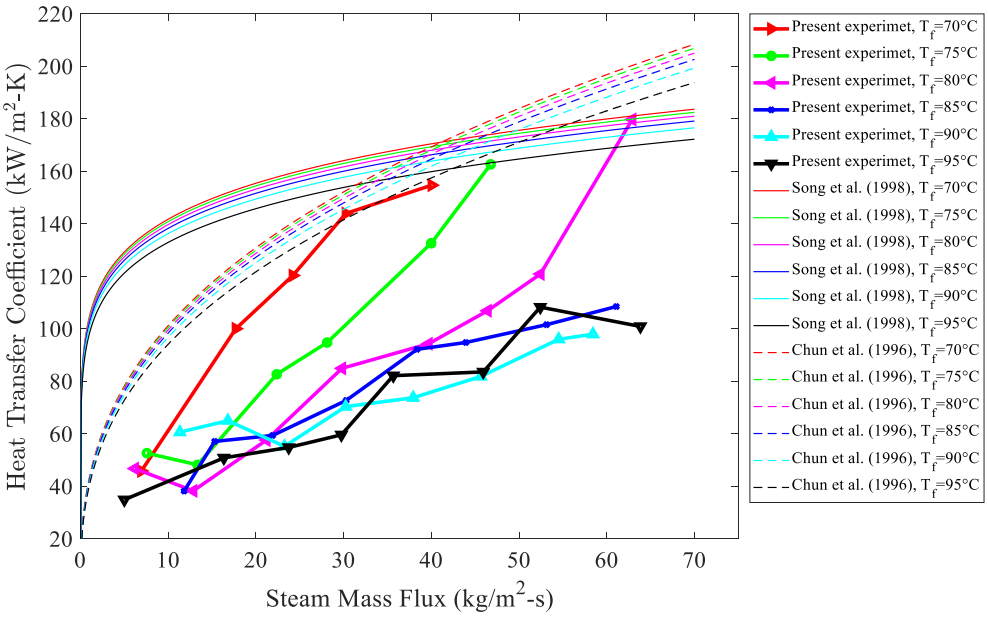

Figure 25. Heat transfer coefficient vs. Steam mass flux with Song *et el.* (1998) and Chun *et el.* (1996)

The heat transfer coefficient proposed by Song *et al*. (1998) is derived as following:

$$h = 1.4453 \cdot c_{PL} G_m B^{0.03587} \left(\frac{G}{G_m} \right)^{0.13315} \tag{9}$$

Chun *et al*. (1996)'s values are also calculated as following:

$$h = 1.3583 \cdot c_{PL} G_m B^{0.0405} \left(\frac{G}{G_m} \right)^{0.3714} \tag{10}$$

where c_{PL} is the specific heat of the liquid in J/kg·K, G_m is the mean value of the steam mass flux in kg/m^2·s (G_m was modified to 30 kg/m^2·s in order to project into the steam mass flux region of the current study), B is the condensation driving potential same as $c_p\left(T_s - T_f\right)/\left(h_s - h_f\right)$, G is the steam mass flux in kg/m^2·s.

Similar to the present study, the empirical correlations of Song *et al*. (1998) and Chun *et al.* (1996) tend to increase the heat transfer coefficient as the steam mass flux increases. As the pool temperature increases, however, the amount of decrease in the heat transfer coefficient is insignificant relatively. This is because the driving potential B containing the temperature variables is so small (0.03587 and 0.0405) that it does not affect the heat transfer coefficient calculation significantly. Song *et al*. (1998) stated in their paper that the major variable in the direct contact condensation for energy transport is the steam mass flux. Kim *et al*. (2004) also mentioned in their paper like that the heat transfer coefficient of the direct contact condensation is not a significant function of the temperature of the sub-cooled water. It means that the correlations of Song *et al*. (1998) and Chun *et al.* (1996) derived by the experimental data at the high steam mass flux region (≥250 kg/m^2·s) indicate that the steam mass flux is a dominant variable at a high mass flux region, and the temperature change does not act as a significant

factor for the heat transfer. Therefore, it can be considered that those correlations are more suitable at the high steam mass flux region where the stable condensation occurs.

Figure 26 shows the variations of the heat transfer coefficient derived from the current study to the pool temperature at various steam mass flux.

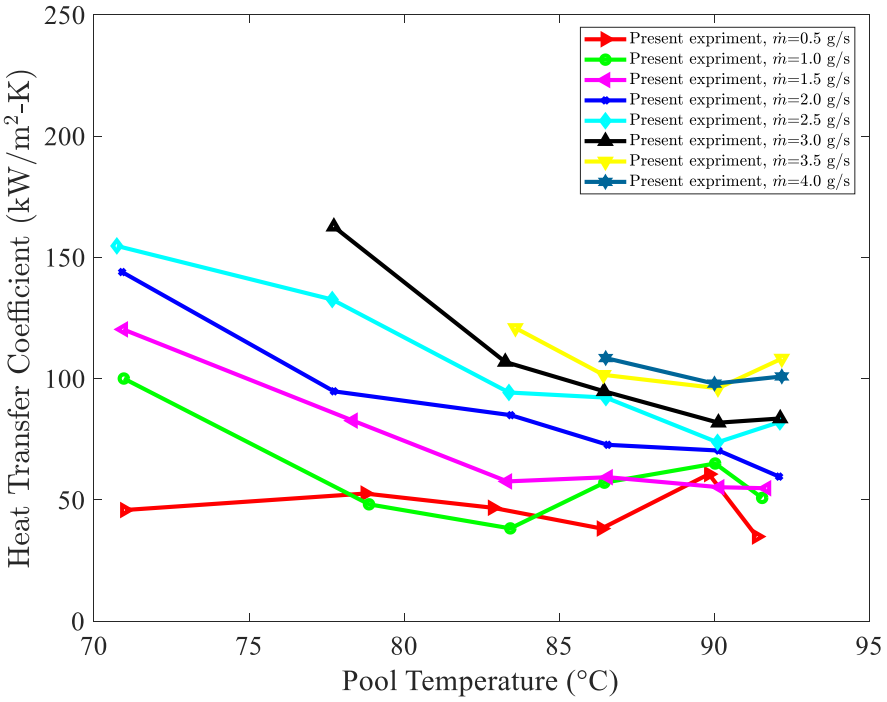

Figure 26. Heat transfer coefficient vs. Pool temperature

As described above, the effect of the pool temperature, which tends to reduce the heat transfer coefficient in various steam mass flux, also appears as shown in Figure 26. However, a decreasing tendency of the heat transfer coefficient appears to be rather irregular when the pool temperature becomes around 90 °C. This is because the temperature region near 90 °C is the boundary between the bubbling condensation oscillation (BCO) and non-condensation. In other

words, since the temperature difference between the steam and the pool is relatively small, the condensation is not likely to occur or is likely to occur irregularly.

Figure 27 shows the experimental results of the current study including the Fukuda (1981)'s data related to the heat transfer coefficient.

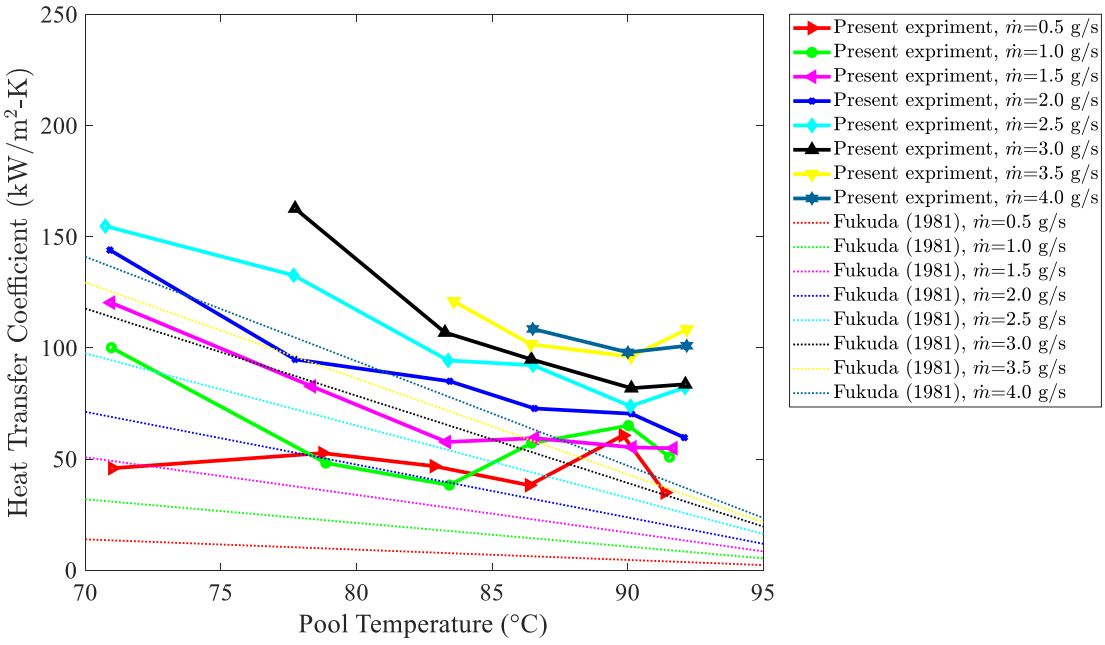

Figure 27. Heat transfer coefficient vs. Pool temperature with Fukuda (1981)

The two studies are not perfectly matched, but it can be reported that the tendency of the heat transfer coefficient is similar as the steam mass flux and the pool temperature change considering that the regions of the steam mass flux of those experiments were different.

Figure 28 shows the experimental results of the current study including the correlations proposed by Song *et al*. (1998) and Chun *et al*. (1996) related to the heat transfer coefficient.

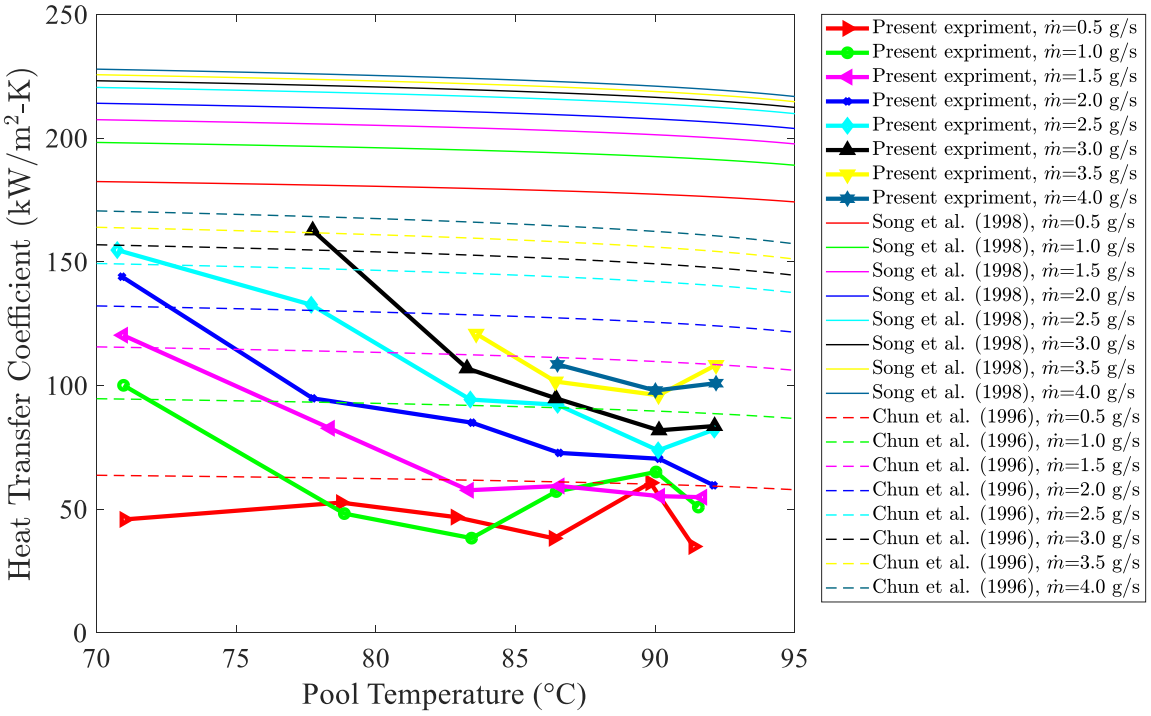

Figure 28. Heat transfer coefficient vs. Pool temperature with Song *et el.* (1998) and Chun *et el.* (1996)

As explained, in Song *et al*. (1998) and Chun *et al.* (1996) studies, the heat transfer coefficient apparently increases as the steam mass flux increases like the current study, but the decrease in the heat transfer coefficient is very small as the pool temperature increases. In addition, generally the heat transfer coefficient values of Song *et al*. (1998) are larger than Chun *et al.* (1996)'s result. This is because the value of the steam mass flux proposed Song *et al*. (1998) is larger than Chun *et al.* (1996) as shown in Eq. (9) and (10).

4.2 Temperature Distribution

As mentioned in the introduction section, most of the previous studies related to steam-water direct contact condensation have measured the pool temperature with thermocouples. In

the current study, however, the pool temperature is measured by two methods which are thermocouples and LIF technique.

As shown in Figure 17, there are ten K-type thermocouples around the nozzle. Figure 29 presents the pool temperature data measured by those thermocouples at the steam mass flux of 1.0 g/s.

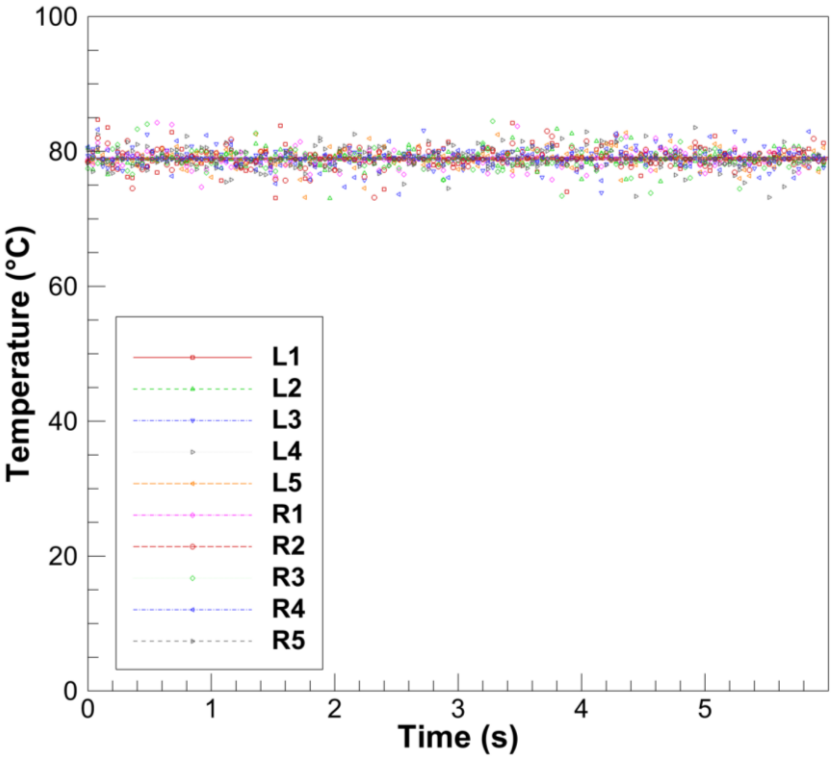

Figure 29. Pool temperature measured by thermocouples ($\dot{m}$: 1.0 g/s)

The averaged pool temperature measured for six seconds is about 78.87 °C. The averaged pool temperatures measured by the thermocouples at the various steam mass flux are used as the reference temperatures for obtaining the properties related to the heat transfer such as the heat flux and the heat transfer coefficient. However, it is difficult to show the local heat transfer and

corresponding temperature changes at the moment of the condensation between the steam and the water using the time-averaged temperatures only. Therefore, in this study, the temperature field of the pool is measured and visualized using LIF technique. Figure 30 represents the raw images of the single period of the steam at the steam mass flux of 1.0 g/s and shows the contour images.

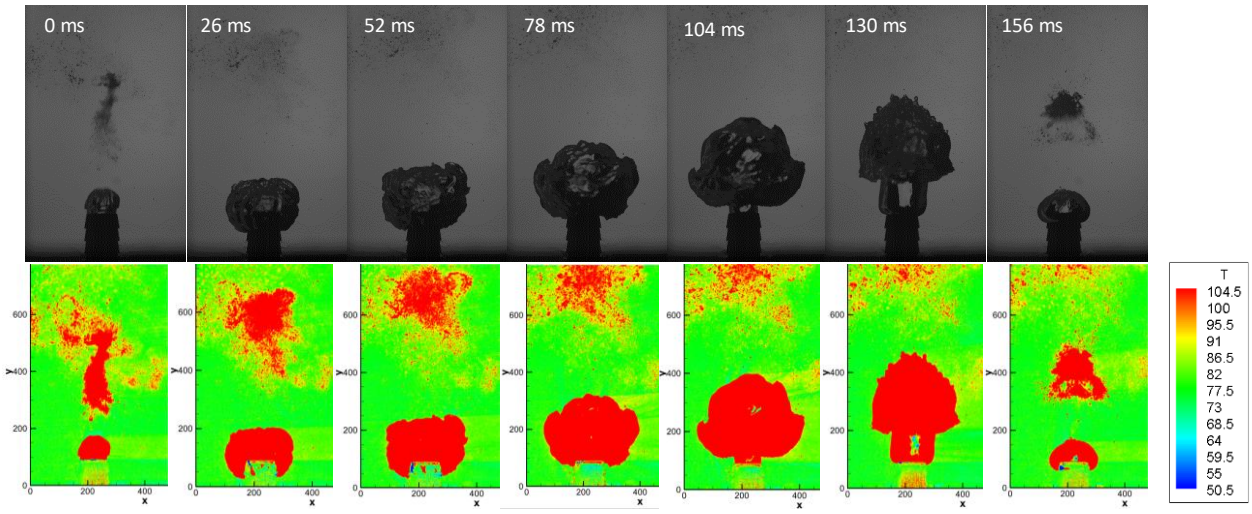

Figure 30. Raw (up) and contour (down) images of single period of steam ($\dot{m}$: 1.0 g/s)

The instantaneous changes of the pool temperature are visualized from the bubble generation of the bubble collapse through LIF technique. In other words, the local temperature is analyzed and visualized at the point where the condensation occurs.

In the same conditions as Figure 30, each of 1,000 raw images taken for a second using a high-speed camera is calibrated, and the calibrated images of 1,000 are averaged by time. Figure 31 presents the time averaged data to visualize the temperature field of the pool after calibration

and shows six x-lines and four y-line for data sampling of the pool. The axis of X and y represent the pixel numbers. Pixel to length conversion factor was 0.98 mm/pixel (100 pixels = 98 mm).

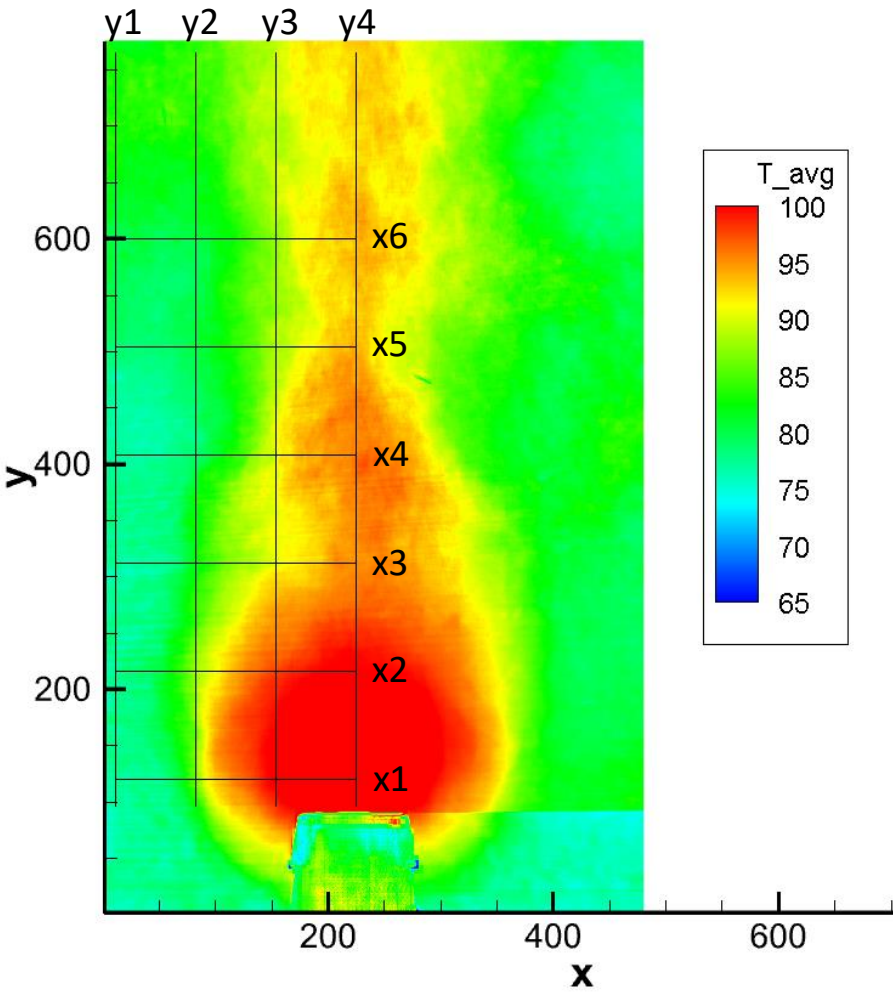

Figure 31. Time-averaged temperature field and sampling lines ($\dot{m}$: 1.0 g/s)

The pool temperature field shows a symmetric trend around the nozzle centerline approximately. Also, the maximum temperature is located where the most frequent condensation occurs.

In Figure 32 and Figure 33, further details on the time-averaged temperature for the specific location can be found. Figure 32 shows the temperature profiles on the extracted lines x1-x6. The line x1 is located at the top, and the line x6 is located at the bottom.

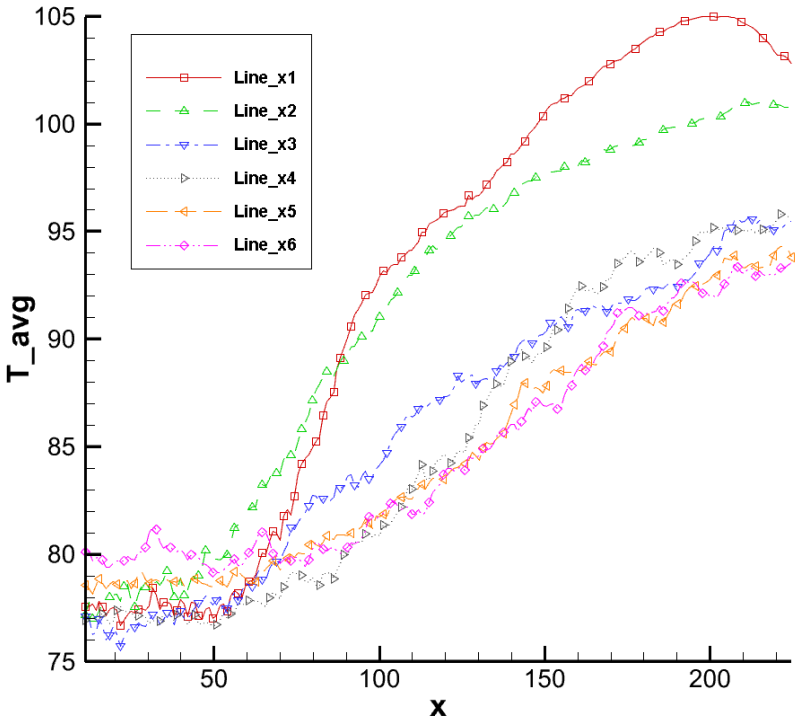

Figure 32. Temperature profiles extracted on x-axis lines

The maximum temperature increases near the nozzle, and the average temperatures tend to decrease as the distance from the nozzle increases. This is because most condensations occur intensively in the vicinity of the nozzle, which means the heat of the steam is transferred to the water. Note that the x-axis represents the left half side of the region of interest. The center of the nozzle is located at x=221 pixel. Also, considering the thermocouples location as shown in Figure 17, the averaged temperature values measure by LIF method could be validated. This is

because the average temperatures of lines x1-x6 below 50 of x axis measured by LIF method are located between 76 °C and 80 °C, which is similar to thermocouples' average temperature (78.87 °C). Figure 33 presents the temperature profiles on the extracted lines y1-y4.

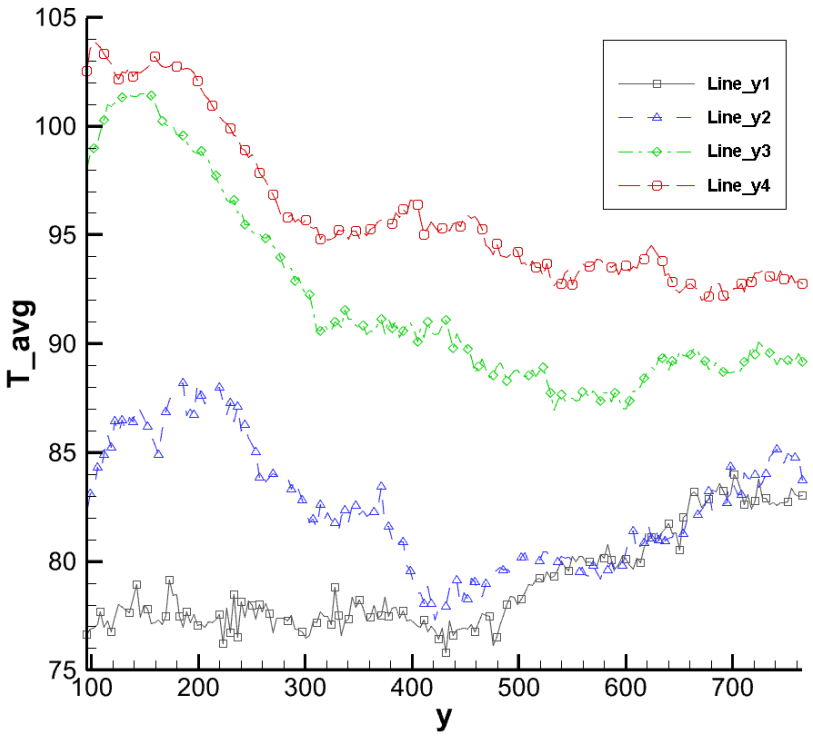

Figure 33. Temperature profiles extracted on y-axis lines

The maximum temperature appears near the nozzle, which is the line y4 located at the center of the nozzle, and the time-averaged temperature far from the nozzle has the lowest value. Given that the average temperature of the water is 78.87 °C in this case, especially the temperatures extracted on the lines of y3 and y4 around the nozzle are all above the average temperature measured by thermocouples. The temperatures of y1 and y2 may mean the

temperature near the steam before condensation occurs, and at y3 and y4, the temperatures mean the heated water temperature due to steam-water direct contact condensation. Therefore, it can be suggested that in case of calculating the local heat transfer coefficient, it is better to use the local water temperature value derived from LIF rather than the average temperature through the thermocouple.

In addition, experimental data sets about the temperature distribution in the pool can be utilized for validation and verification of computational fluid dynamics (CFD). Kang and Song (2007), for example, studied a CFD analysis for thermal mixing of a steam discharged from a sparger in a subcooled water. Especially, a CFD analysis on temperature change of the entire water tank is described. Thus, it can be suggested that the experimental temperature data of current study could be used to verify and validate this CFD analysis on temperature field in the pool.

4.3 Bubble Equivalent Diameter

As mentioned in the methodology section, for the deeper understanding of the steam condensation, the bubble's equivalent diameter of the wetted surface is calculated using Eq. (11) when the steam condensation occurs.

$$D_{b,eq} = \sqrt{\frac{4A_b}{\pi}} \tag{11}$$

Figure 34 presents the photographs of a single period of a bubble using a high-speed camera at the steam flow rate of 1.0 g/s when the pool temperature increases.

(a) T_f : 70°C, $\dot{m}$: 1.0 g/s

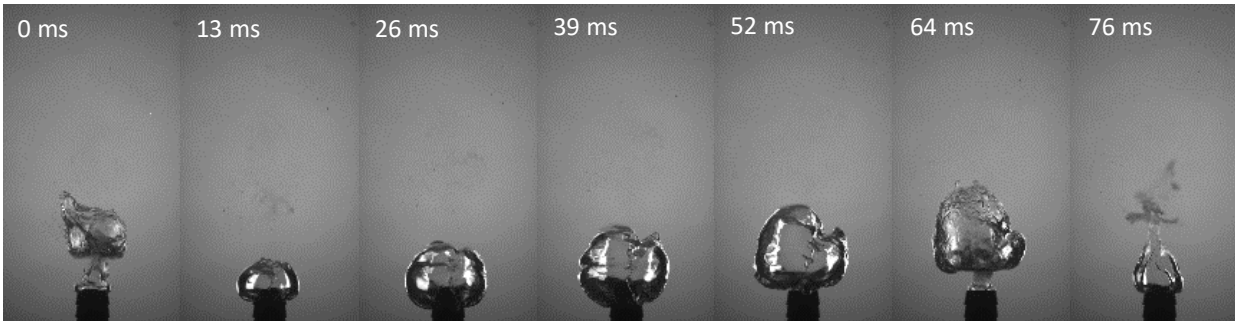

(b) T_f : 80°C, $\dot{m}$: 1.0 g/s

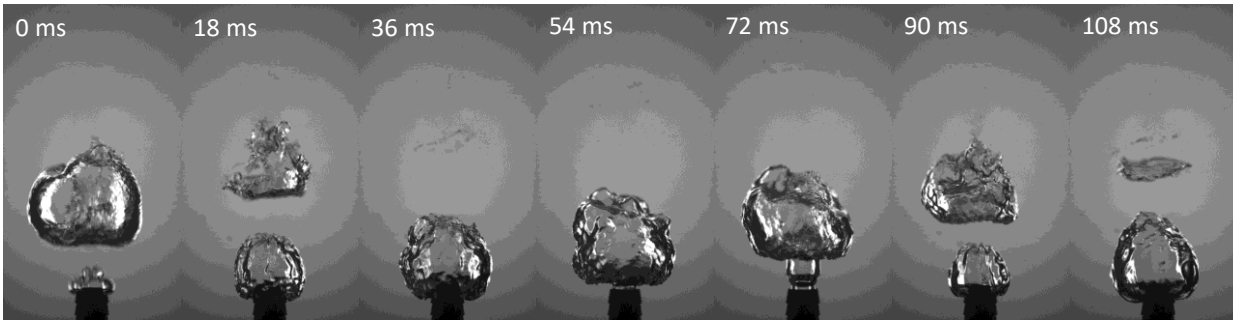

(c) T_f : 90°C, $\dot{m}$: 1.0 g/s

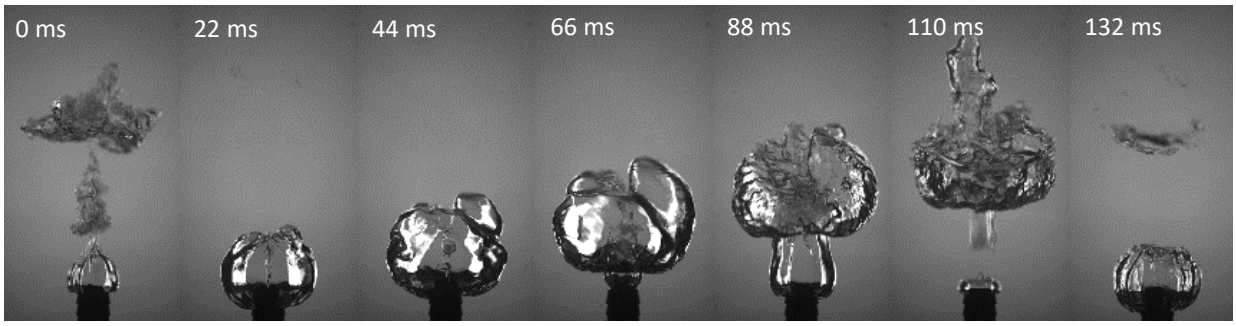

Figure 34. High-speed camera photos of a single period of bubble with increase of the pool temperature

The bubble size increases with increase of the pool temperature at the same flow rate (1.0 g/s) as shown in Figure 34. Also, it can be found that the internal of condensation becomes

slower as the temperature increases as shown at the time of a single period. It means that the increase in the pool temperature affects the condensation time as well as the bubble size.

Figure 35 shows the analysis of the bubble equivalent diameter as pool temperature increases by the various steam flow rates.

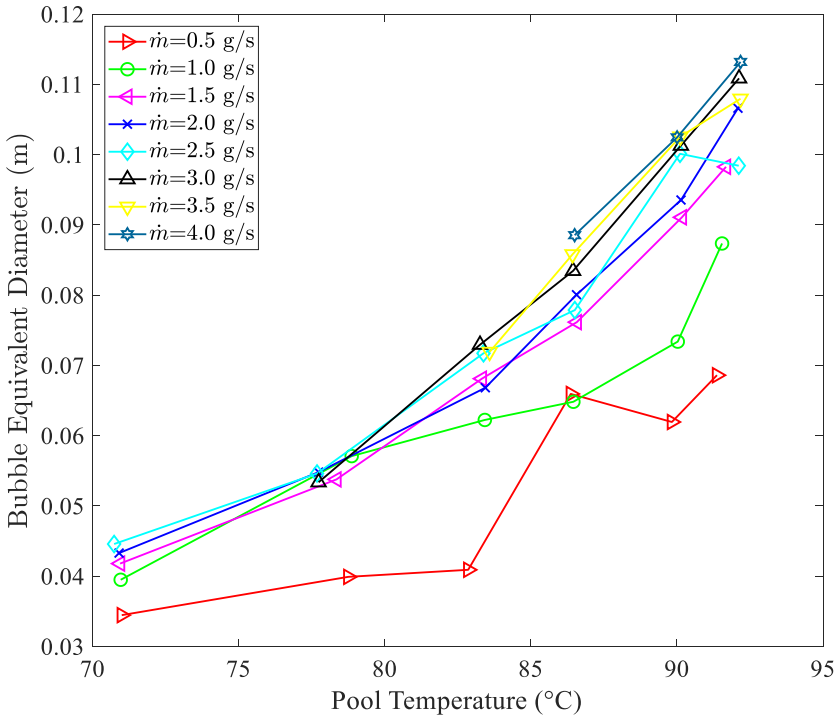

Figure 35. Bubble equivalent diameter vs. Pool temperature

The bubble equivalent diameter is evaluated in range of 0.033-0.114 m. The bubble equivalent diameter tends to increase as the temperature and the steam flow rate increase. This is because the heat transfer rate decreases as the temperature difference of the steam and the pool decreases.

The photos of a single period of a bubble using a high-speed camera at the pool temperature of 85°C when the steam flow rate increases are shown in Figure 36.

(a) T_f : 85 °C, $\dot{m}$: 1.0 g/s

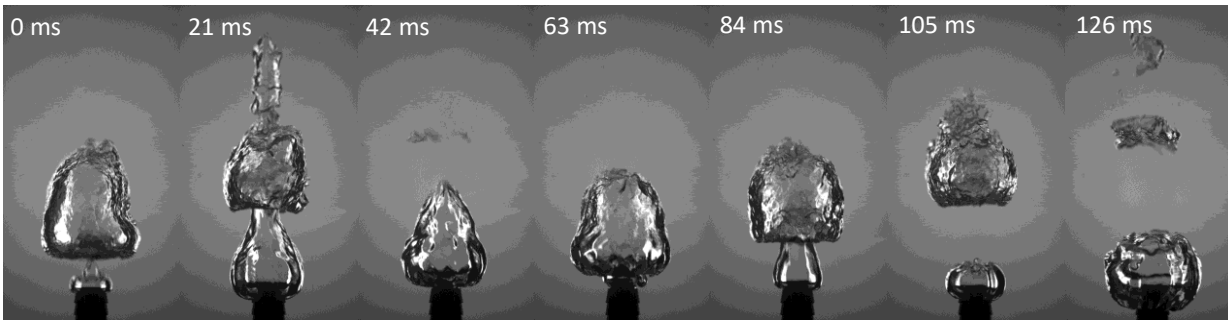

(b) T_f : 85 °C, $\dot{m}$: 2.0 g/s

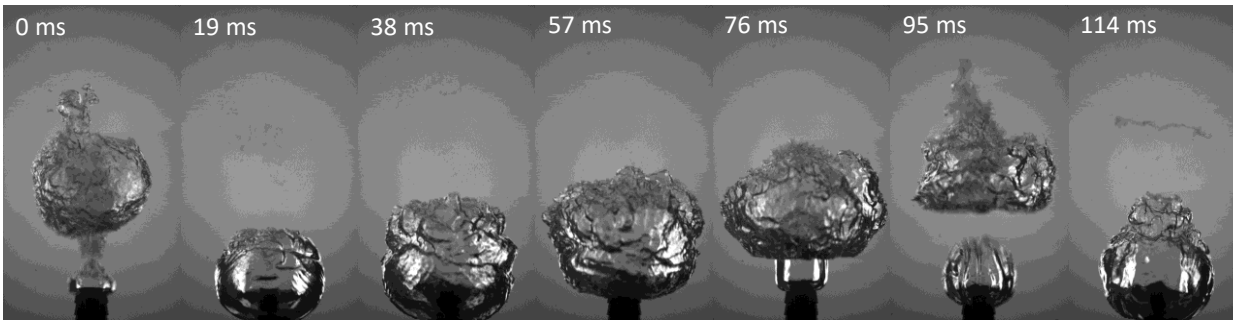

(c) T_f : 85 °C, $\dot{m}$: 3.0 g/s

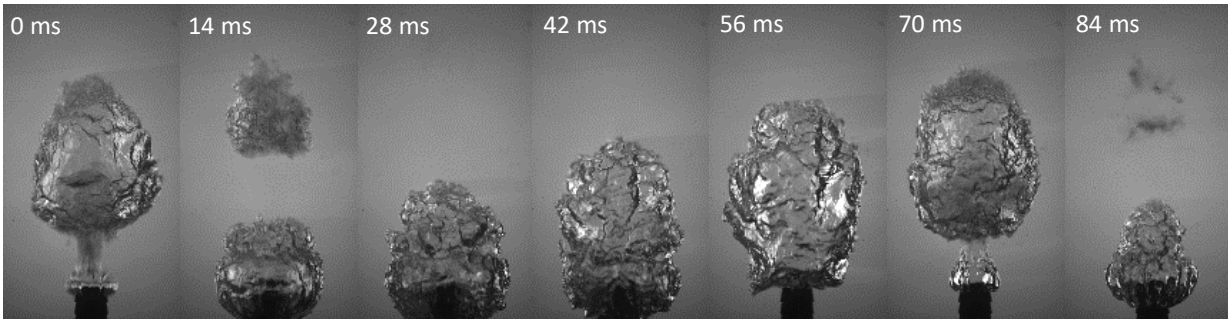

Figure 36. High speed camera photos of a single period of bubbles with increase of the steam mass flow rate

The size of the bubble increases with increasing flow rate at the same temperature. However, it can be found that a single period of steam condensation is further shortened. This is because the heat transfer rate increases as the steam flow rate increases at the same temperature. Therefore, steam condensation occurs quickly since the heat transfer increases.

The analysis of the bubble equivalent diameter as pool temperature increases by the various steam flow rates is presented in Figure 37.

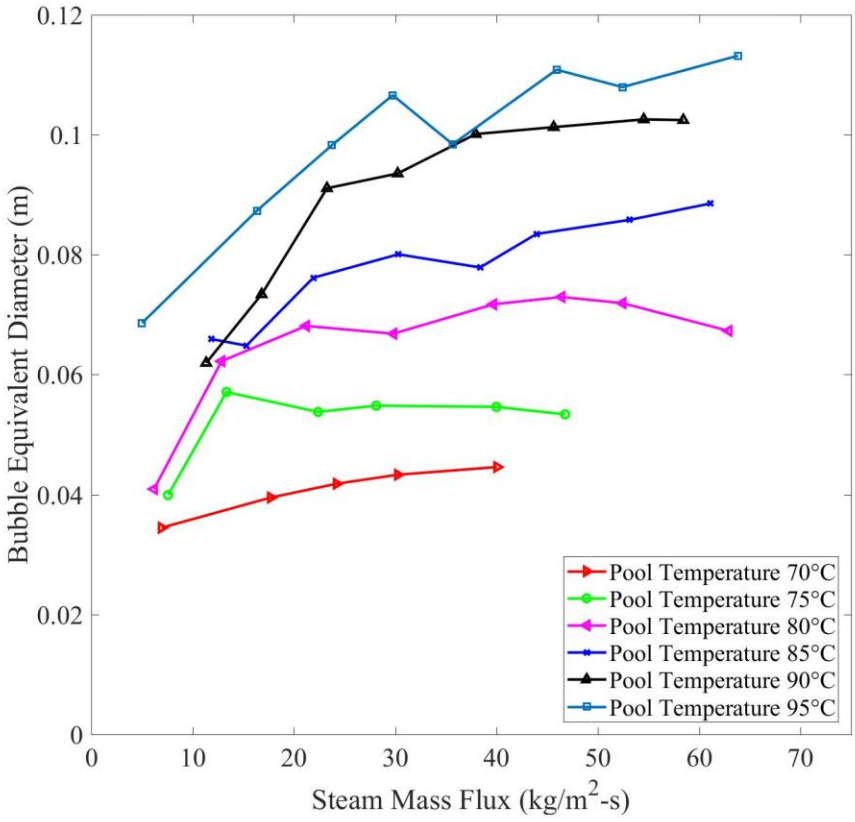

Figure 37. Bubble equivalent diameter vs. Steam mass flux

The tendency of increase of the bubble equivalent diameter is distinguished clearly as the pool temperature increases. The bubble equivalent diameter, however, initially increases, and then tends to converge to a certain diameter as the steam mass flux increases. Considering that the maximum steam mass flux is 65 $kg/m^2 \cdot s$, the convergence of the diameter is related to the transition of the condensation regime from the unstable condensation to the stable condensation. It means that the form of the steam changes from an isolated bubble to a stable jet as the regime is changed from condensation oscillations to steady condensation region.

In the high steam mass flux region where a stable condensation occurs, the hydraulic characteristics of the bubble have been investigated through a jet modeling to derive a l/d (length/diameter) correlation, since the shape of the bubble ejected from the nozzle is like a jet rather than an isolated bubble.

Thus, an isolated bubble modeling is also required in the unstable condensation region where the current study is performed, like the jet modeling in the stable condensation. Although the bubble modeling is not developed in the present study, experimental data on the bubble equivalent diameter could be used for modeling studies in future.

5. CONCLUSION

The experiments of the steam-water direct contact condensation in subcooled water have been conducted to study the characteristics of the heat transfer. Especially the heat transfer coefficient, the temperature distribution and the bubble equivalent diameter have been investigated at pool temperatures of 70-95°C and with steam mass fluxes of 5-65 kg/m^2·s. The essential properties required to calculate them have been measured using LIF method and the image processing technique. The averaged heat transfer coefficient derived by the image processing is found in a range of 24.57-179.78 kW/m^2-K. Compared to previous studies, current study has similar tendency with the correlation of the heat transfer coefficient proposed by Fukuda (1981), which has high sensitivity on both the pool temperature and the steam mass flux in the unstable condensation region, while it seems to be different with the correlations of the heat transfer coefficient suggested by Song *et al.* (1998) and Chun *et al.* (1996). This is because they conducted the experiments in stable condensation region and concluded that the steam mass flux is the major controlling variable for heat transfer at the high mass flux region. The pool temperature distribution visualized by LIF shows that local heat transfer resolved by time in entire pool, which could be utilized to calculate the local heat transfer coefficient. The bubble equivalent diameter is evaluated in range of 0.033-0.114 m. The bubble equivalent diameter initially increases as the steam mass flux, and then tends to converge from the point where the condensation regime is changed from unstable region to stable region. Based on the experimental data and the analysis, the results are summarized as follows:

1. The heat transfer coefficient of steam-water direct contact condensation in the unstable region has a high sensitivity on both the pool temperature and the steam mass flux.

2. The laser-induced fluorescence (LIF) could be utilized for analyzing the local heat transfer characteristics, since the time-averaged temperature field of the entire pool is visualized, and the information of local temperature is obtained.
3. The bubble equivalent diameter of unstable isolated bubble initially increases as the steam mass flux increases, and then tends to converge due to the regime change from the unstable to the stable condensation. Thus, for deeper understanding about the hydraulic characteristics of the steam bubble in the unstable condensation region, an isolated bubble modeling is required like a jet modeling in the stable condensation region.

Finally, it is expected that the experimental data of the current study such as the temperature distribution and bubble equivalent diameter would be utilized for the validation and verification of computational fluid dynamics (CFD) analysis on a temperature field of a pool and for the bubble modeling in the unstable condensation region.

REFERENCES

[1] Kerney P. J., G. M. Faeth, and D. R. Olson, “Penetration characteristics of a submerged steam jet.” *AIChE Journal* 18.3 (1972): 548-553.

[2] Brucker, G. G., and E. M. Sparrow. “Direct contact condensation of steam bubbles in water at high pressure.” *International Journal of Heat and Mass Transfer* 20.4 (1977): 371-381.

[3] Fukuda, S., “Pressure Variations due to Vapor Condensation in Liquid, (II) Phenomena at Large Vapor Mass Flow Flux.” *Nippon Genshiryoku Gakkai-Shi* (Japanese) 24 (1981): 466-474.

[4] Su, T. M., “Suppression Pool Temperature Limits for BWR Containments.” *United States Nuclear Regulatory Commission* NUREG-0783 (1981).

[5] Simpson, M. E., and C. K. Chan. “Hydrodynamics of a subsonic vapor jet in subcooled liquid.” *Journal of Heat Transfer* 104 (1982): 271-278.

[6] Nariai, Hideki and Izuo Aya, “Fluid and pressure oscillations occurring at direct contact condensation of steam flow with cold water.” *Nuclear Engineering and Design* 95 (1986): 35-45.

[7] Ali M. A., J. Moghaddasi, and Samir A. Ahmed, “Examination of temperature effects on the lasing characteristics of rhodamine cw dye lasers.” *Applied Optics* 29.27 (1990): 3945-3949.

[8] Jeje, Ayodeji, Benjamin Asante, and Brian Ross, “Steam bubbling regimes and direct contact condensation heat transfer in highly subcooled water.” *Chemical Engineering Science* 45.3 (1990): 639-650.

[9] Aya, Izuo and Hideki Nariai, “Evaluation of heat transfer coefficient at direct-contact condensation of cold water and steam.” *Nuclear Engineering and Design* 131 (1991):17-24.

[10] Lahey, R. T. and F. J. Moody, “The Thermal Hydraulics of a Boiling Water Reactor-Second Edition.” *American Nuclear Society* (1993).

[11] Chun, Moon-Hyun, Yeon-Sik Kim, and Jee-Won Park, “An investigation of direct condensation of steam jet in subcooled water.” *International Communications in Heat and Mass Transfer* 23 (1996): 947-958.

[12] Song, Chul-Hwa, Seok Cho, Hwan-Yeol Kim, Yoon-Young Bae, and Moon-Ki Chung, “Characterization of direct contact condensation of steam jets discharging into a subcooled water.” *IAEA-TECDOC* 1145 (1998): 21-37.

[13] Sakakibara J. and R. J. Adrian, “Whole field measurement of temperature in water using two-color laser induced fluorescence.” *Experiments in Fluids* 26 (1999): 7-15.

[14] Lavieille P., F. Lemoine, G. Lavergne, J. F. Virepinte, and M. Lebouche, “Temperature measurements on droplets in monodisperse stream using laser-induced fluorescence.” *Experiments in Fluid* 29 (2000): 429-437.

[15] Mark J. Gallina, “Development of a two-color laser-induced florescence based temperature imaging device with micro-scale resolution.” Master’s thesis, Texas A&M University (2002)

[16] Youn, Deok Hyun, Kyung Bo Ko, Young Yeon Lee, Moo Hwan Kim, Youn Young Bae, and Jong Kyun Park, “The direct contact condensation of steam in a pool at low mass flux.” *Journal of Nuclear Science and Technology* 40.10 (2003): 881-885.

[17] Kim, Yeon-Sik, Jee-Won Park, and Chul-Hwa Song, “Investigation of the steam-water direct contact condensation heat transfer coefficients using interfacial transport models.” *International Communications in Heat and Mass Transfer* 31.3 (2004): 397-408.

[18] Kar, Saptarshi, Xiao Dong Chen, and Mark Nelson, “Direct-contact Heat transfer coefficient for condensing vapour bubble in stagnant liquid pool.” *Chemical Engineering Research and Design* 85.3 (2007): 320-328.

[19] Wu, Xin-Zhuang, Jun-Jie Yan, Shu-Feng Shao, Yan Cao, and Ji-Ping Liu, “Experimental study on the condensation of supersonic steam jet submerged in quiescent subcooled water: Steam plume shape and heat transfer” *International Journal of Multiphase Flow* 33 (2007): 1296-1307.

[20] Kim, Yeon-Sik and Yeong-Joong Youn, “Experimental study on turbulent jet condensation through a hole in a water tank.” *International Communications in Heat and Mass Transfer* 35 (2008): 21-29.

[21] Kang, Hyung Seok and Chul Hwa Song, “CFD analysis for thermal mixing in a subcooled water tank under a high steam mass flux discharge condition.” *Nuclear Engineering and Design* 238 (2008): 492-501.

[22] Gulawani, Sagar S., Sachin K. Dahikar, Channamallikarjun S. Mathpati, Jysetharaj B. Joshi, Manish S. Shah, Chaganti S. Ramaprasad, and Daya S. Shukla, “Analysis of flow pattern and heat transfer in direct contact condensation.” *Chemical Engineering and Science* 64.8 (2009): 1719-1738.

[23] Song, Chul-Hwa and Yeon-Sik Kim, “Direct Contact Condensation of Steam Jet in a Pool.” *Advances of Heat Transfer* 43 (2011): 227-288.

[24] Song, Chul-Hwa, Seok Cho, and Hyung-Seok Kang, “Steam Jet Condensation in a Pool: From Fundamental Understanding to Engineering Scale Analysis.” *Journal of Heat Transfer* 134 (2012): 1-15.

[25] Krotiuk, W.J., C. Boyd, T. Zaki, and W. Wang, “BWR ECCS Pump Suction Concerns following a LOCA.” *United States Nuclear Regulatory Commission* NUREG-2196 (2016).

[26] Lee, Saya, Arturo Cabral, Se Ro Yang, Rodolfo Vaghetto, and Yassin A. Hassan, “Steam/Air Condensation Shakedown Test Report.” TAMU-SAC-SDTR-001 (2017).

[27] Yang, Se Ro, Joseph Seo, Kimoon Lee, Rodolfo Vaghetto, and Yassin A. Hassan, “Steam-Water Report - the direct contact condensation of steam jet in subcooled water pool.” TAMU-SAC-SWR-001 (2018).

[28] Yang, Se Ro, Joseph Seo, Kimoon Lee, Rodolfo Vaghetto, and Yassin A. Hassan, “Steam-Water Report - the direct contact condensation of steam and air mixture jet in subcooled water pool.” TAMU-SAC-SWR-002 (2018).

[29] Yang, Se Ro, Joseph Seo, Kimoon Lee, Rodolfo Vaghetto, Duy Thien Nguyen, and Yassin A. Hassan, “Steam-Air-Water Final Report - the direct contact condensation of steam and air mixture jet in subcooled water pool.” TAMU-SAC-FR-001 (2018).

[30] Yang, Se Ro, Joseph Seo, and Yassin A. Hassan, “Thermal hydraulic characteristics of unstable bubbling of direct contact condensation of steam in subcooled water.” *International Journal of Heat and Mass Transfer* 138 (2019): 580-596.

[31] Yang, Se Ro, Joseph Seo, and Yassin A. Hassan, “Spatiotemporally resolved temperature measurement of unstable direct contact condensation of steam in subcooled water using backlight aided planar laser induced fluorescence.” *In Print.*

APPENDIX

“REPRESENTATIVE PHOTOS OF SINGLE PERIOD OF STEAM BUBBLE”

Representative photographs of single periods of the steam bubble using high-speed camera at each pool temperature from 70 to 95 °C and at each steam flow rate from 0.5 to 4.0 g/s are presented as follows.

A. 70 °C

(a) 0.5 g/s

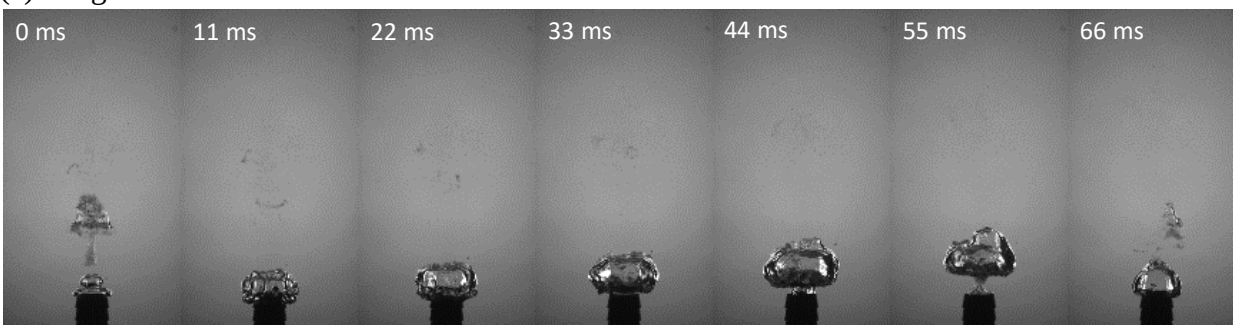

(b) 1.0 g/s

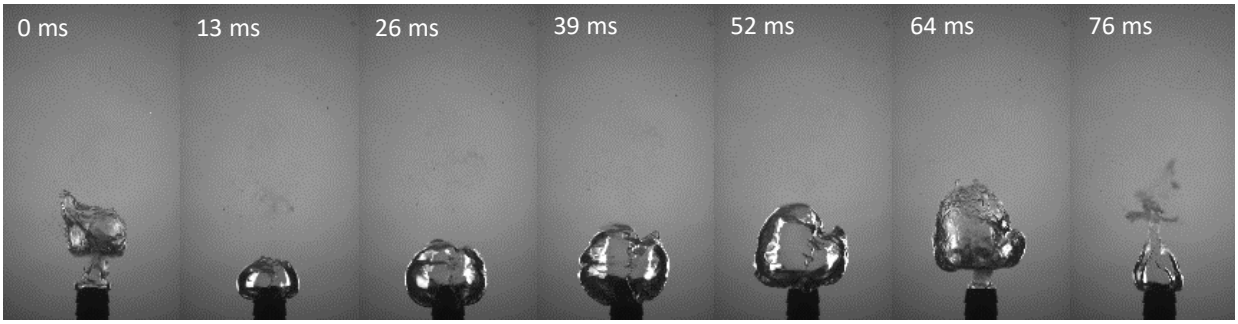

(c) 1.5 g/s

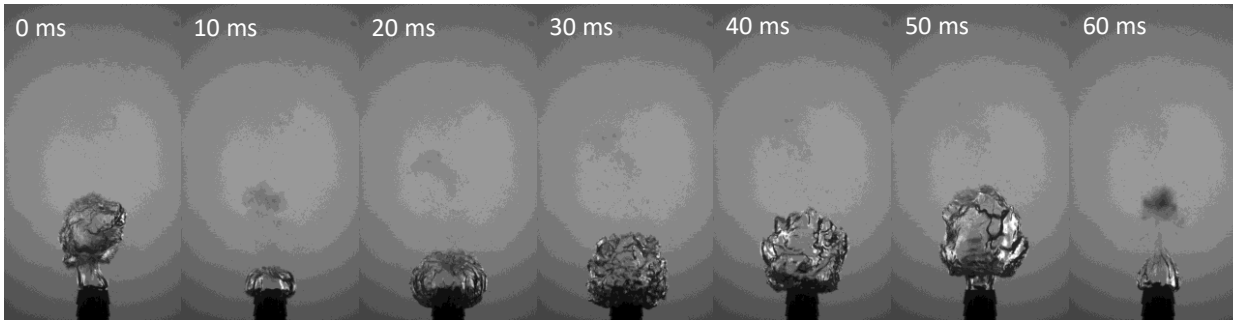

(d) 2.0 g/s

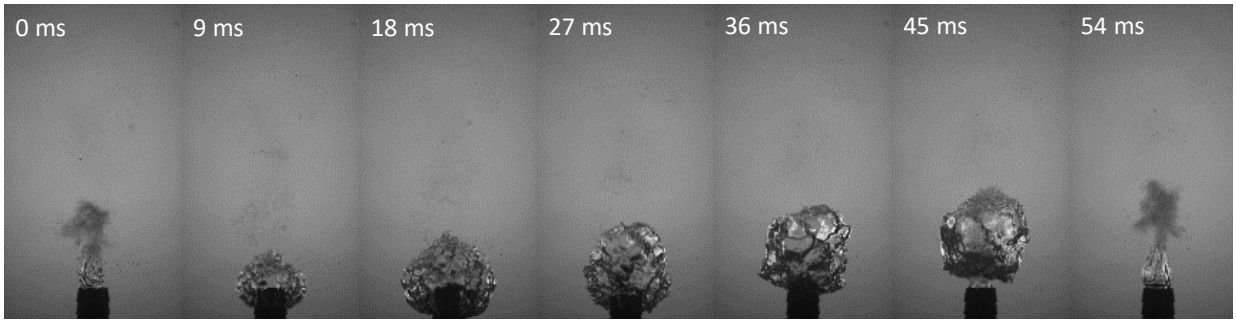

(e) 2.5 g/s

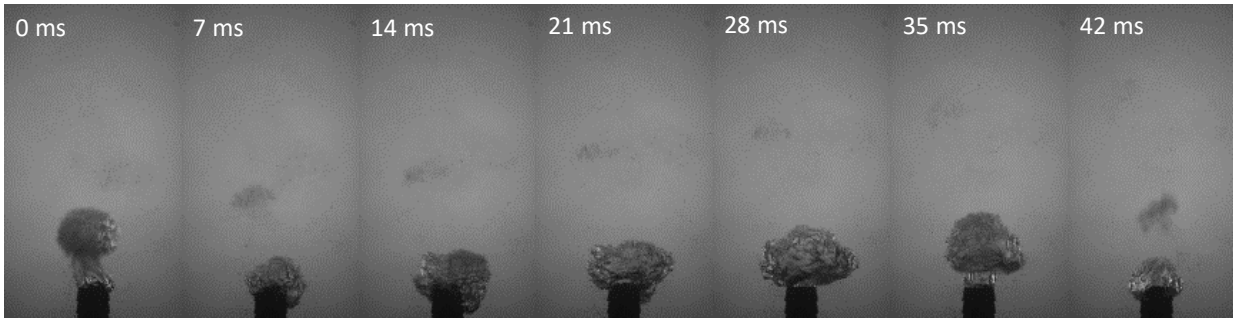

(f) 3.0 g/s

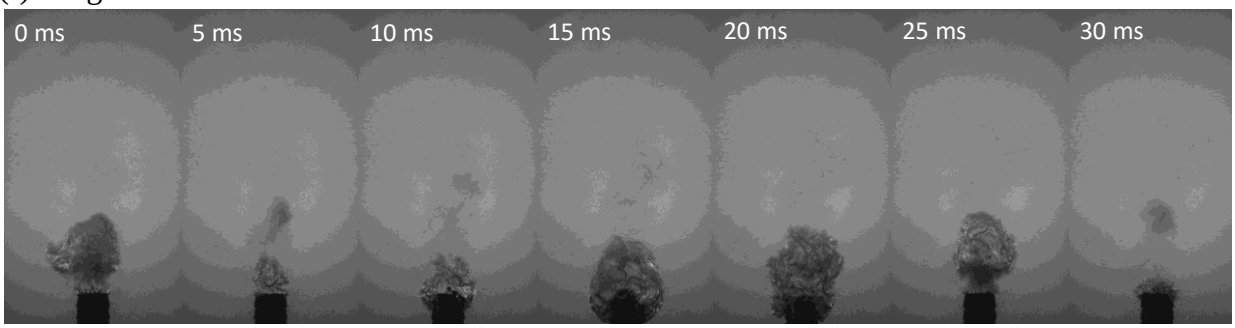

(g) 3.5 g/s

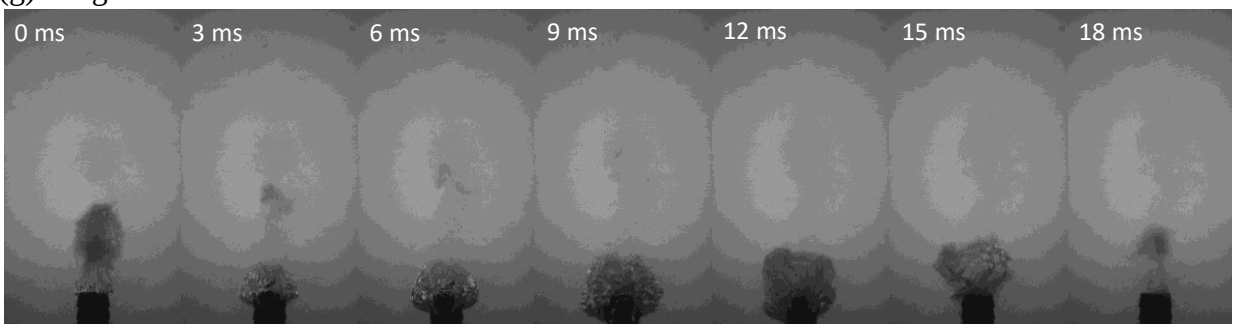

(h) 4.0 g/s

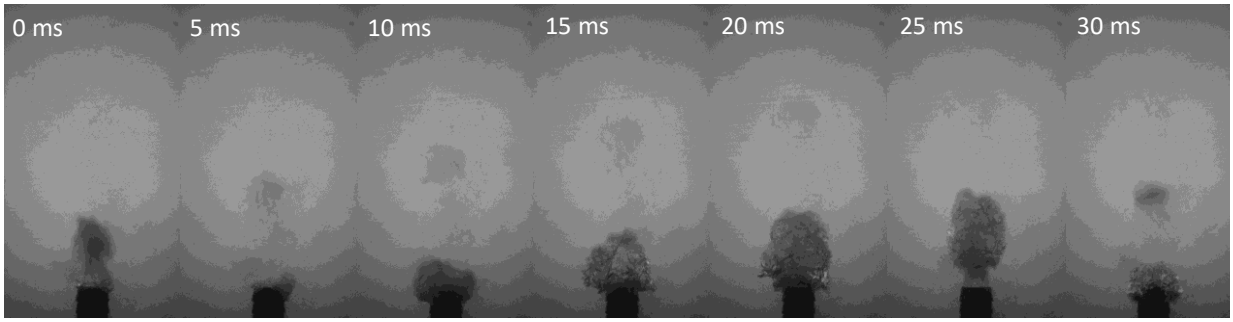

B. 75 °C

(a) 0.5 g/s

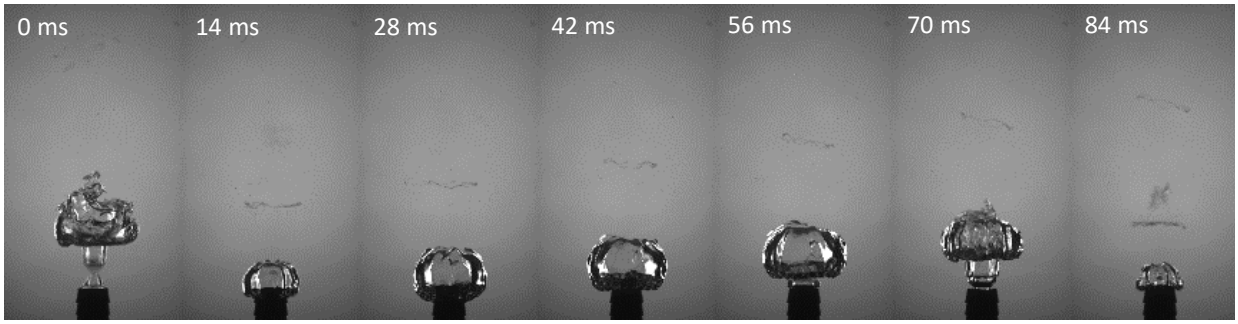

(b) 1.0 g/s

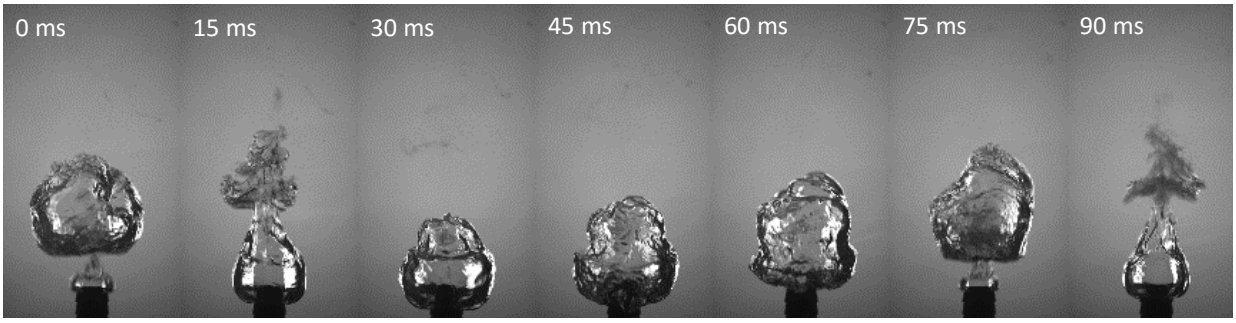

(c) 1.5 g/s

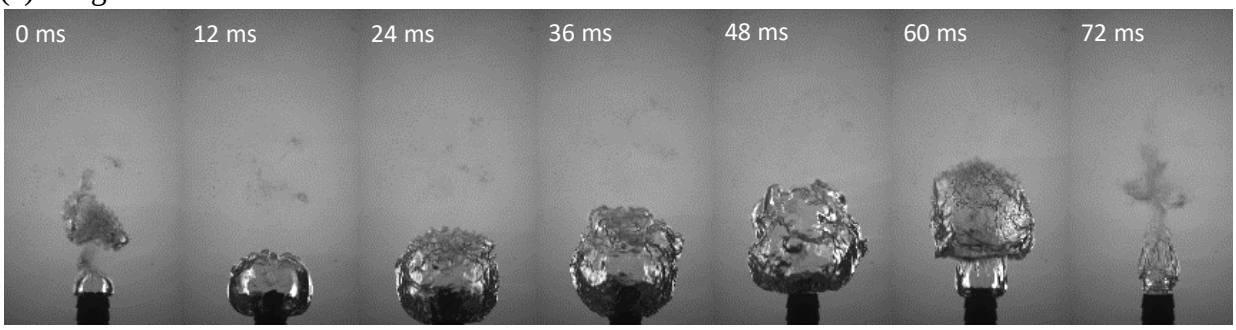

(d) 2.0 g/s

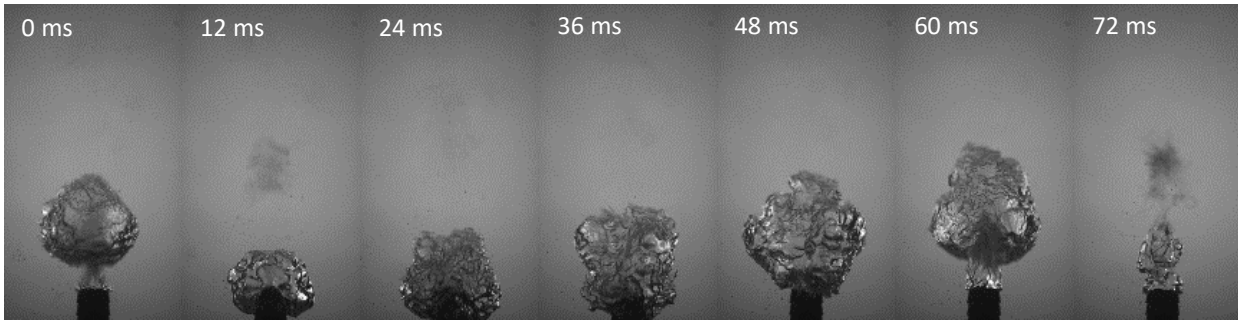

(e) 2.5 g/s

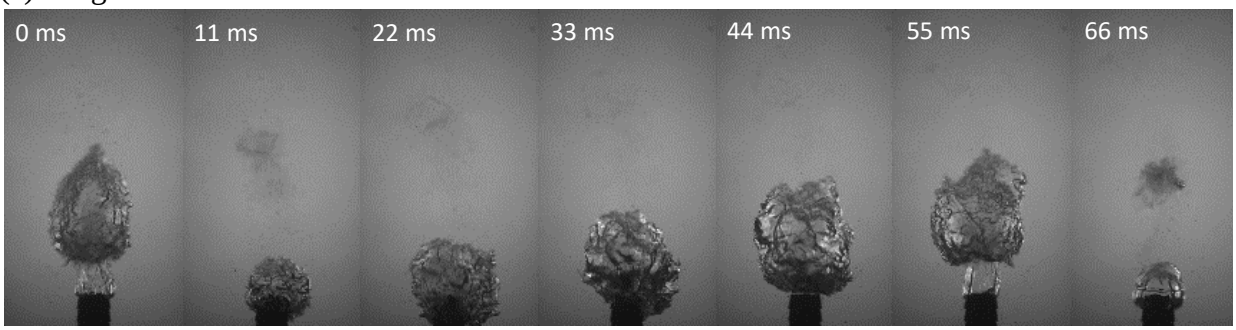

(f) 3.0 g/s

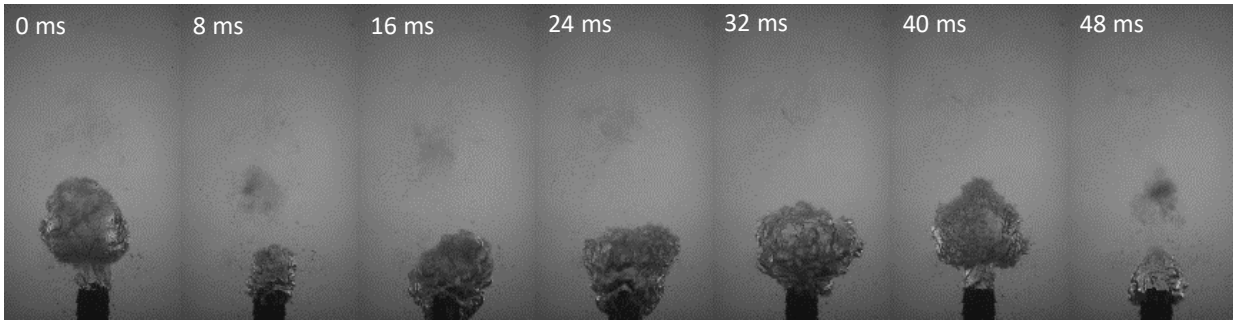

(g) 3.5 g/s

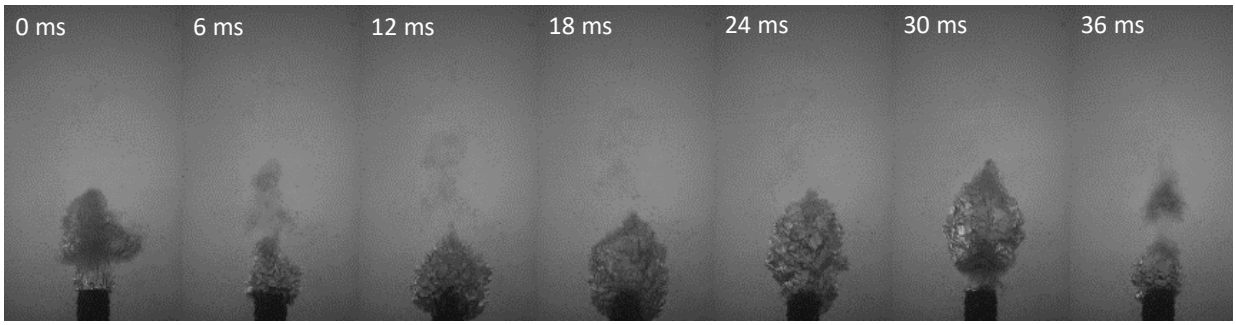

(h) 4.0 g/s

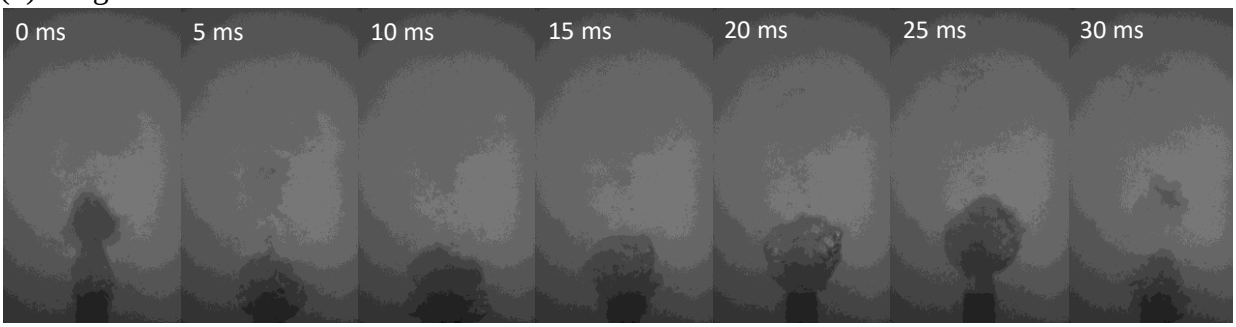

C. 80 °C

(a) 0.5 g/s

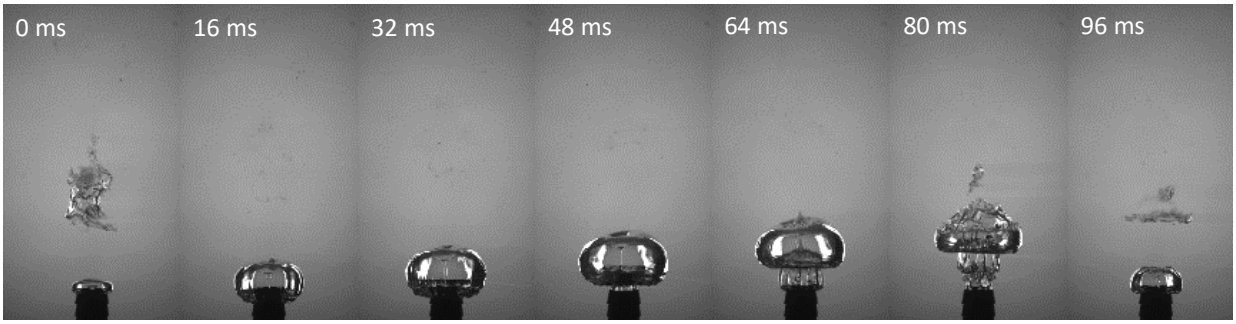

(b) 1.0 g/s

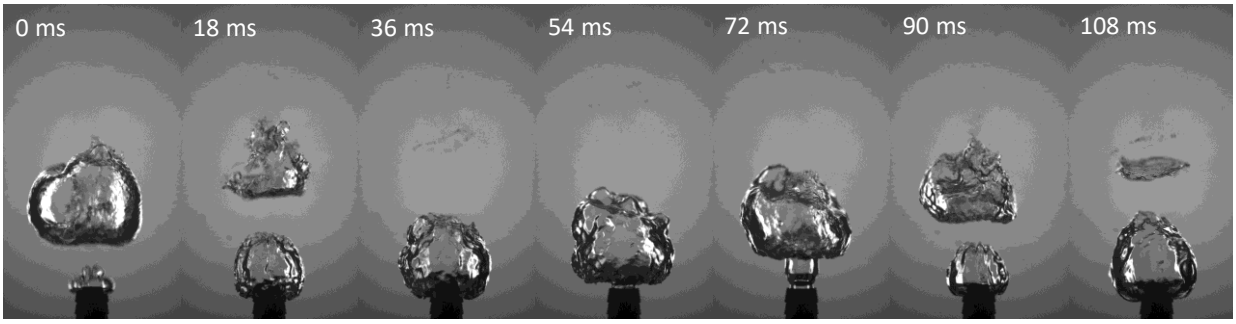

(c) 1.5 g/s

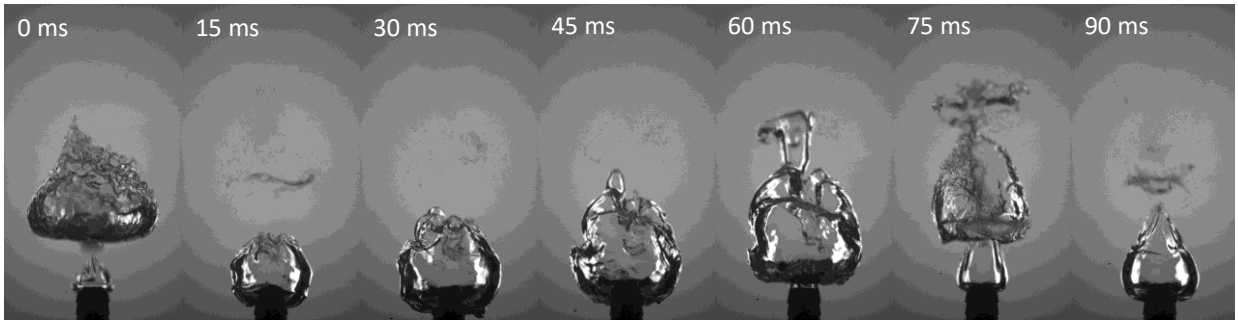

(d) 2.0 g/s

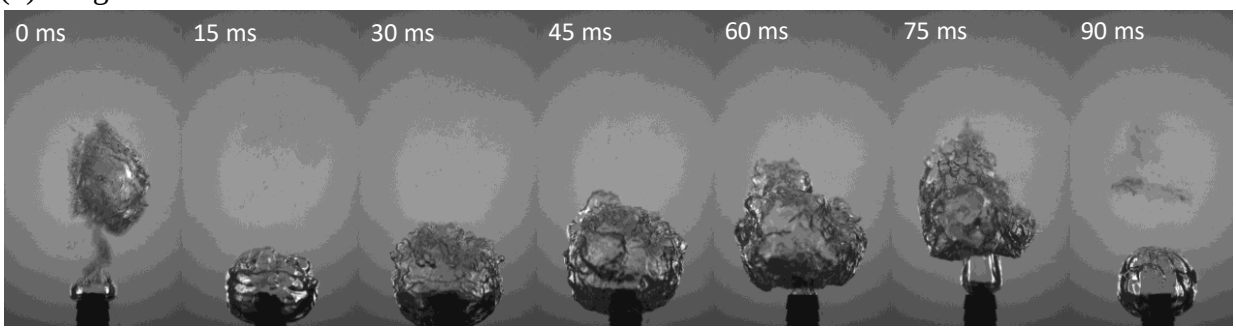

(e) 2.5 g/s

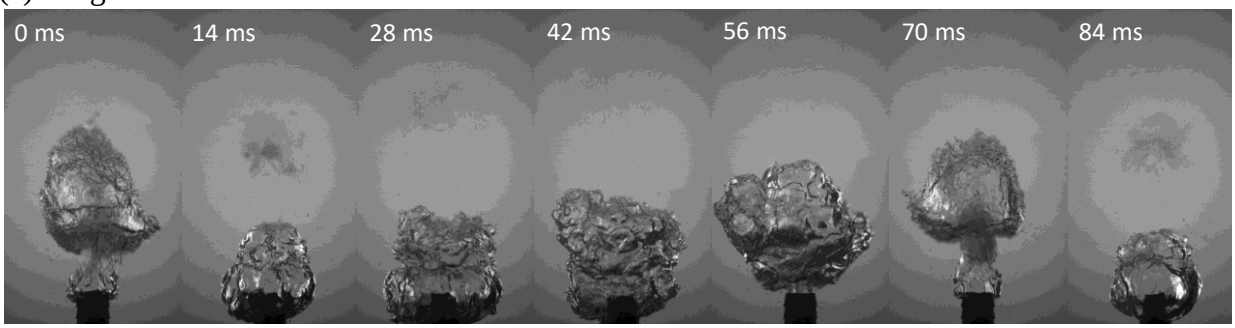

(f) 3.0 g/s

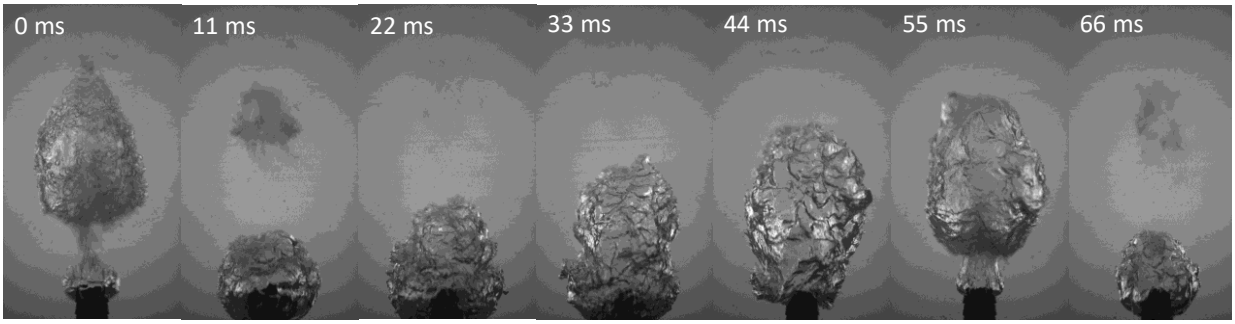

(g) 3.5 g/s

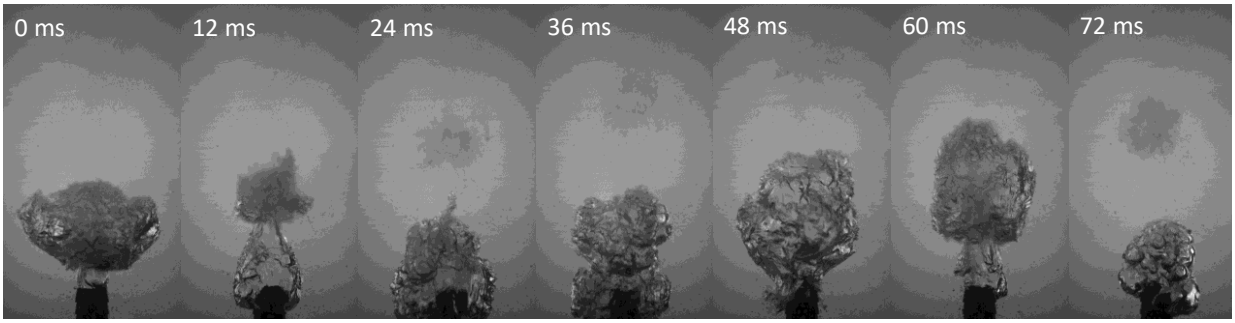

(h) 4.0 g/s

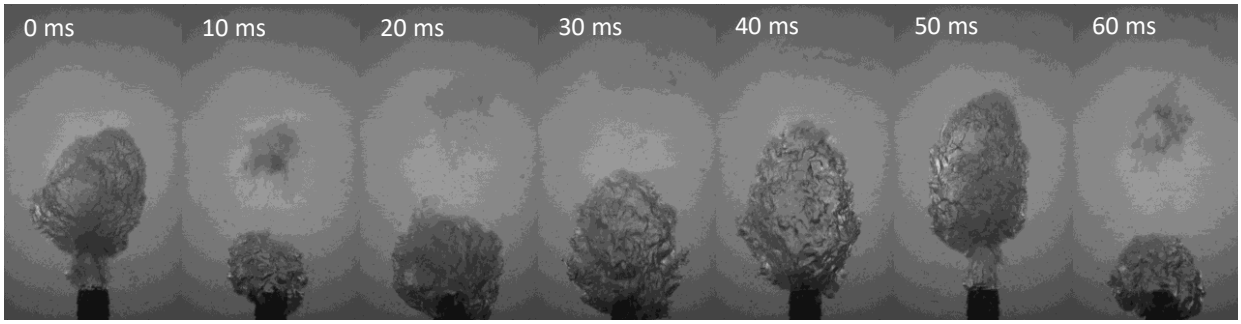

D. 85 ℃

(a) 0.5 g/s

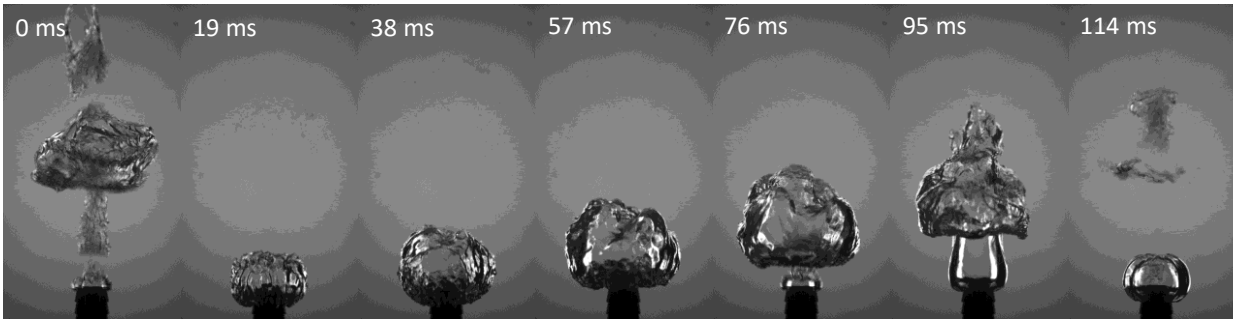

(b) 1.0 g/s

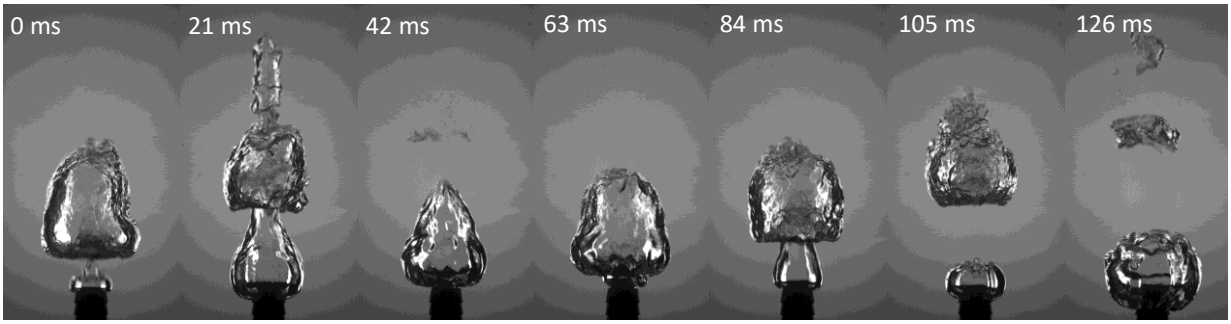

(c) 1.5 g/s

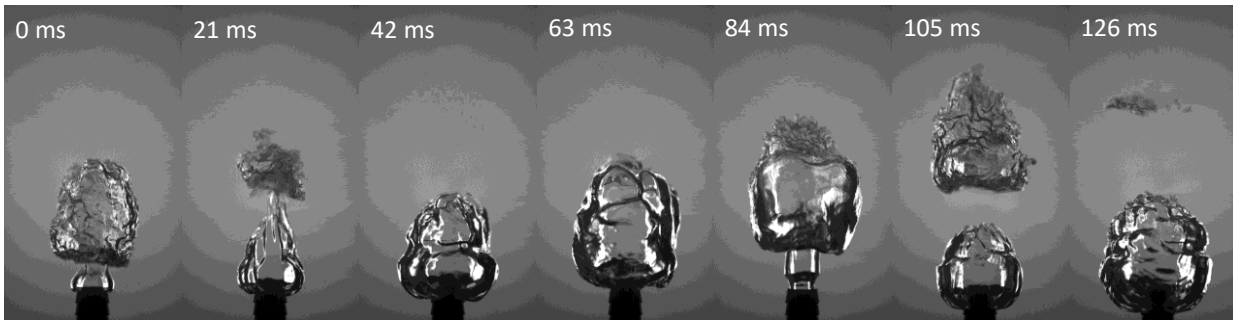

(d) 2.0 g/s

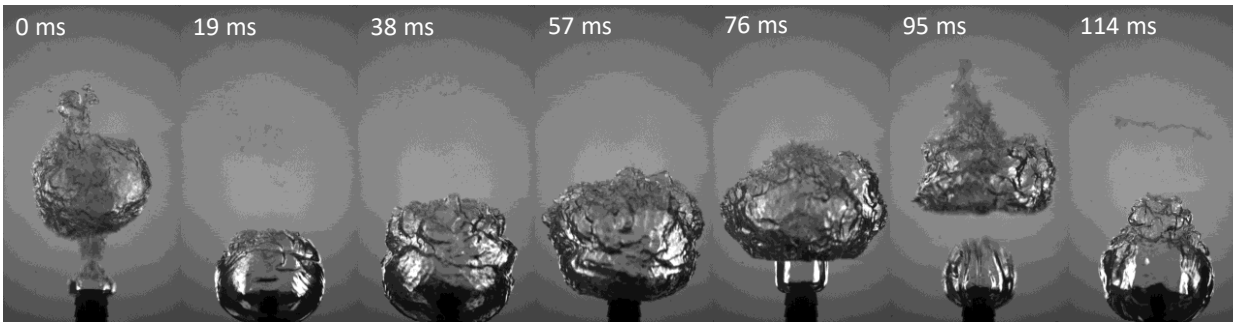

(e) 2.5 g/s

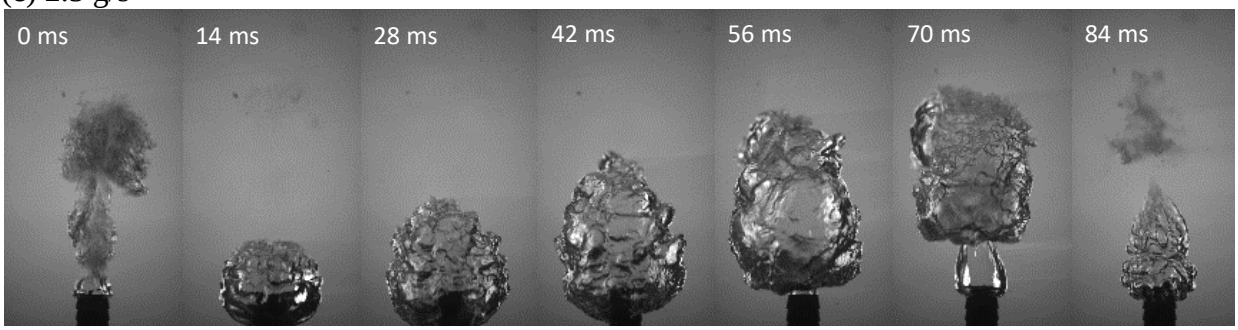

(f) 3.0 g/s

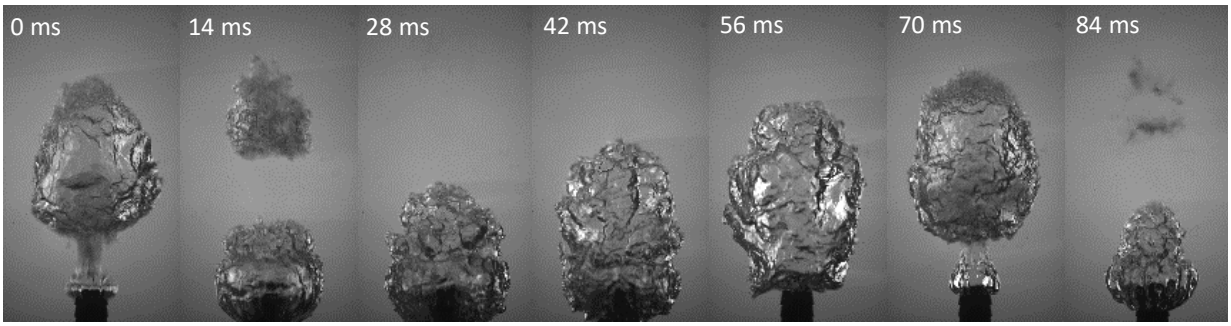

(g) 3.5 g/s

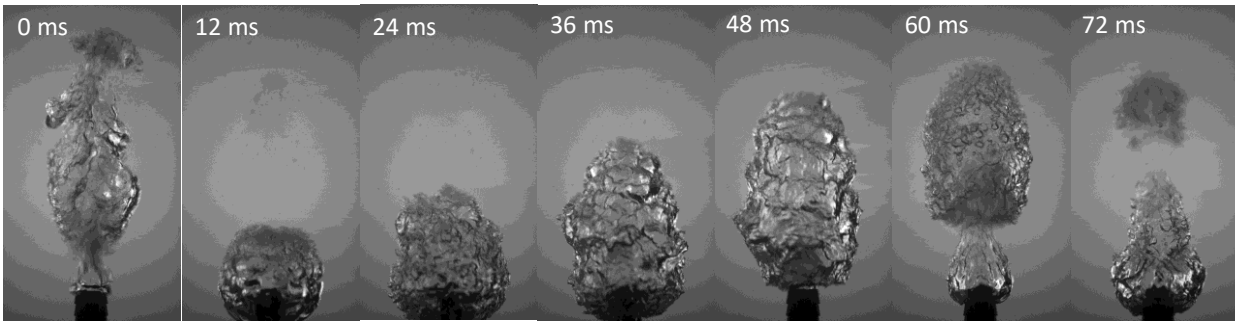

(h) 4.0 g/s

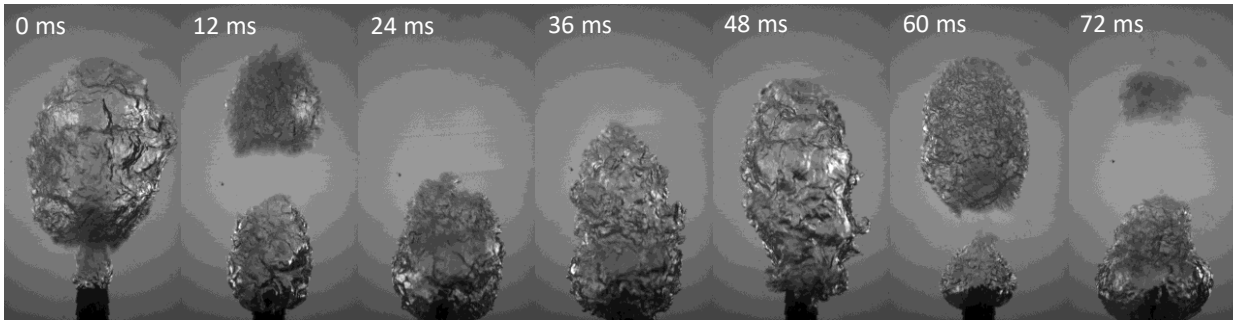

E. 90 °C

(a) 0.5 g/s

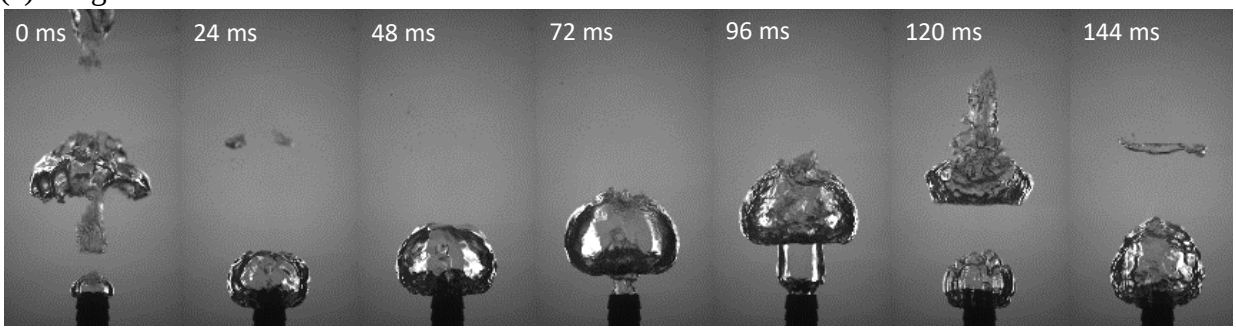

(b) 1.0 g/s

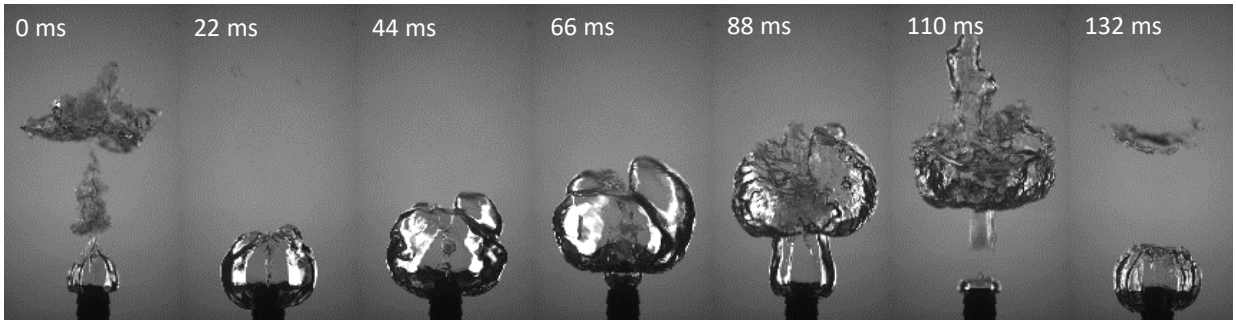

(c) 1.5 g/s

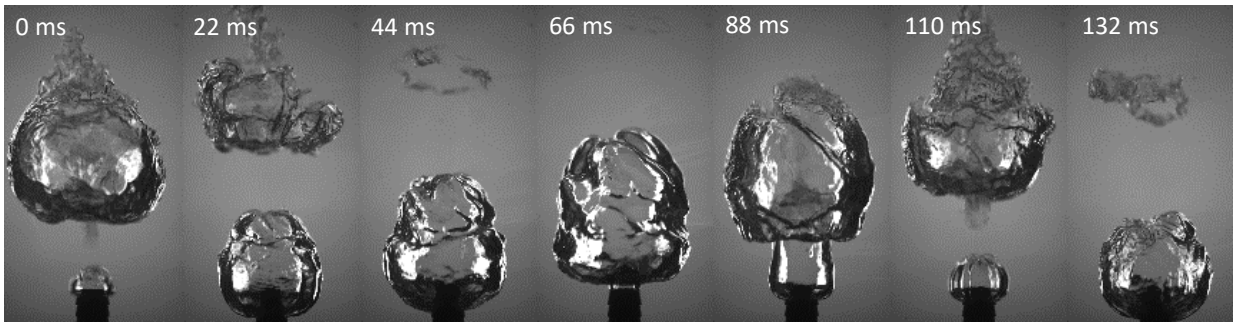

(d) 2.0 g/s

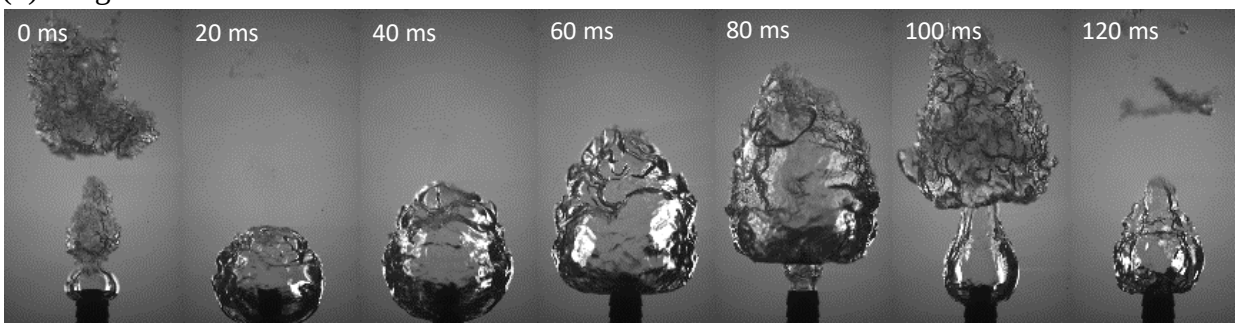

(e) 2.5 g/s

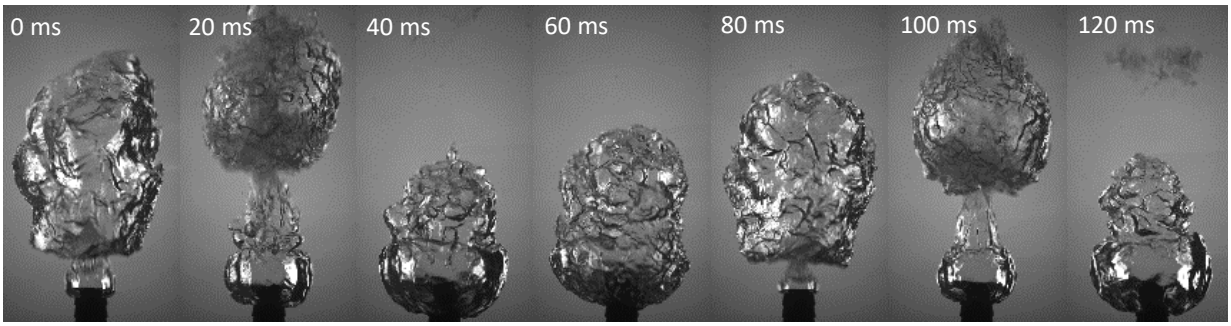

(f) 3.0 g/s

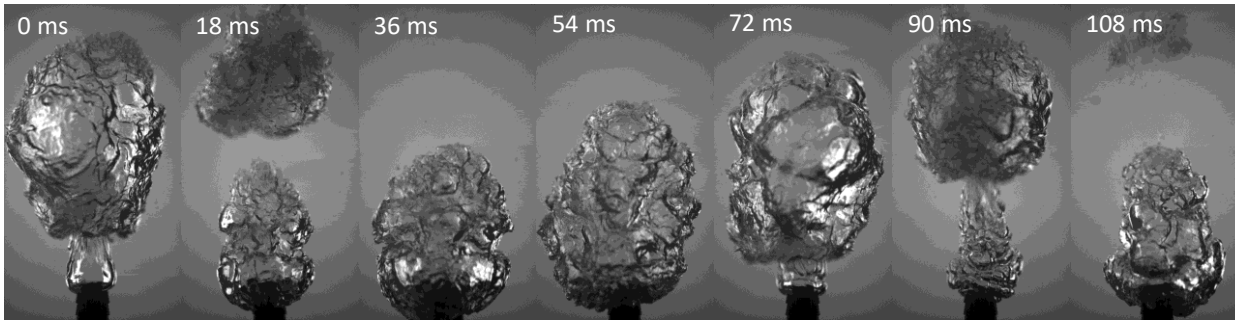

(g) 3.5 g/s

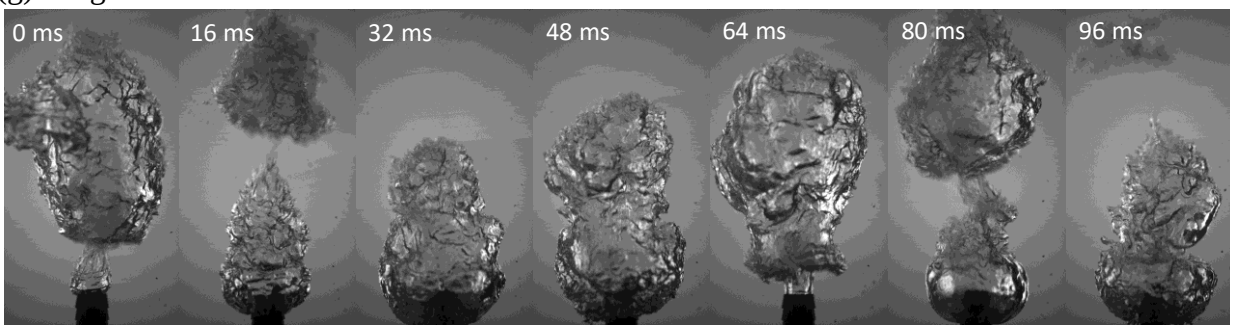

(h) 4.0 g/s

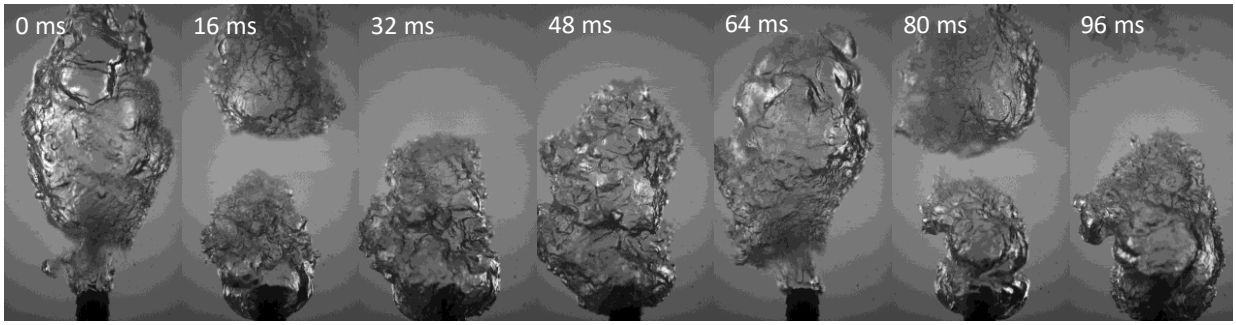

F. 95 ℃

(a) 0.5 g/s

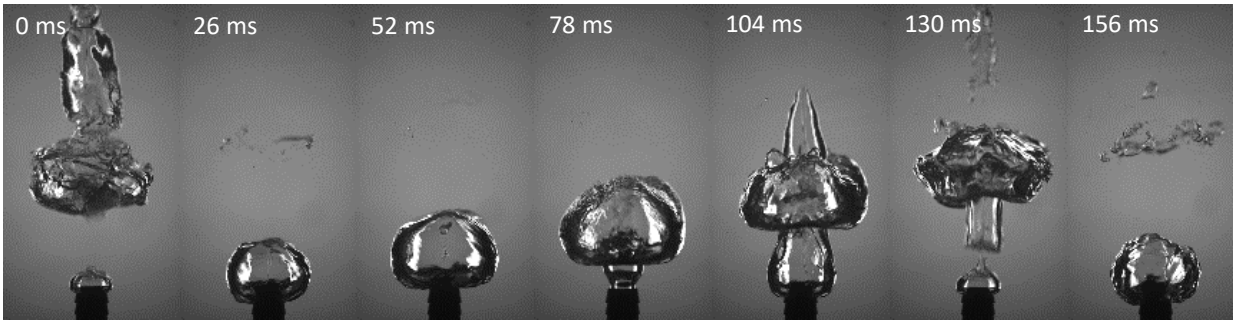

(b) 1.0 g/s

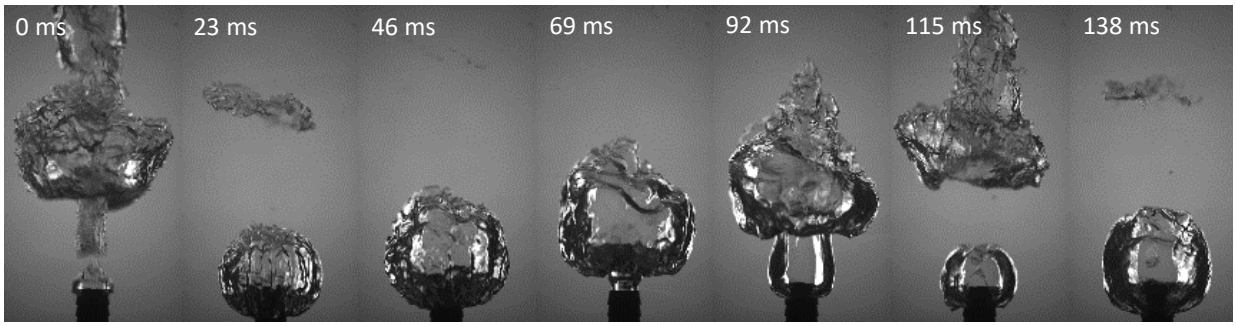

(c) 1.5 g/s

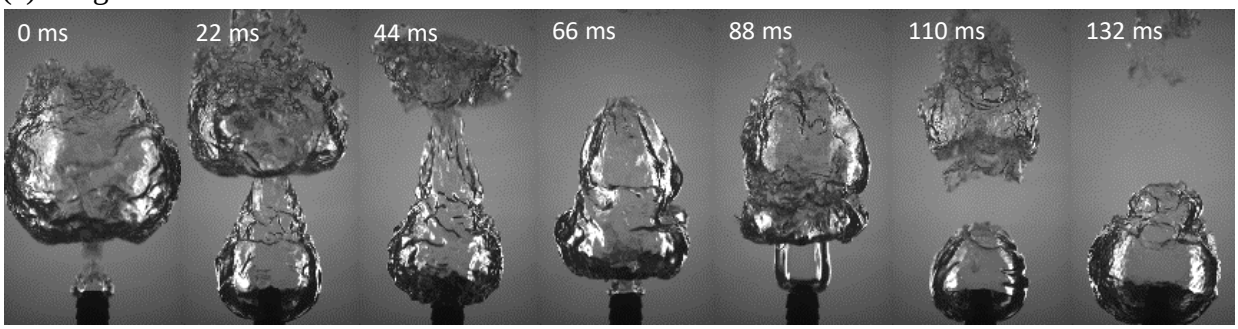

(d) 2.0 g/s

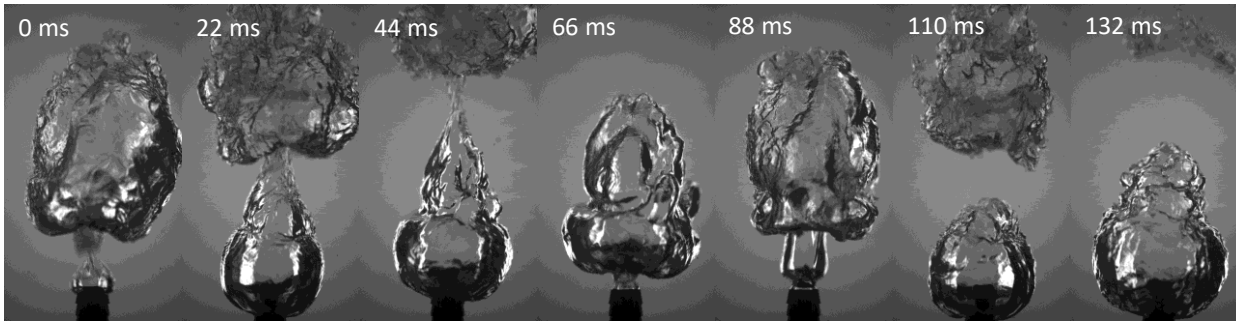

(e) 2.5 g/s

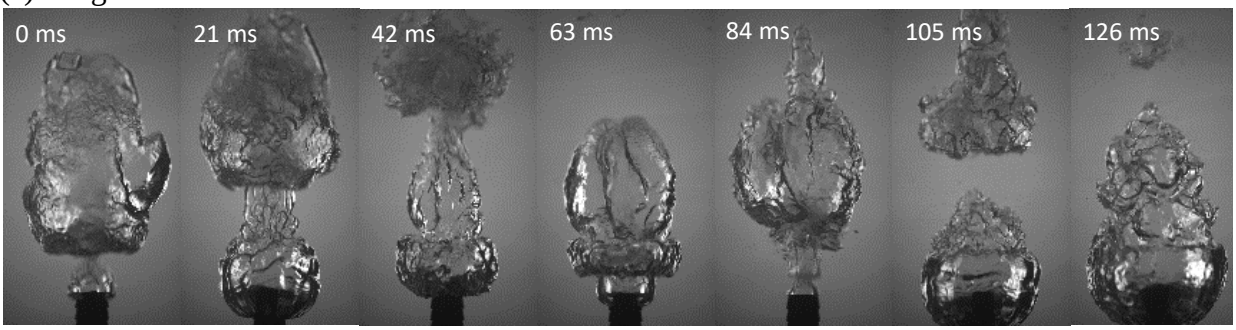

(f) 3.0 g/s

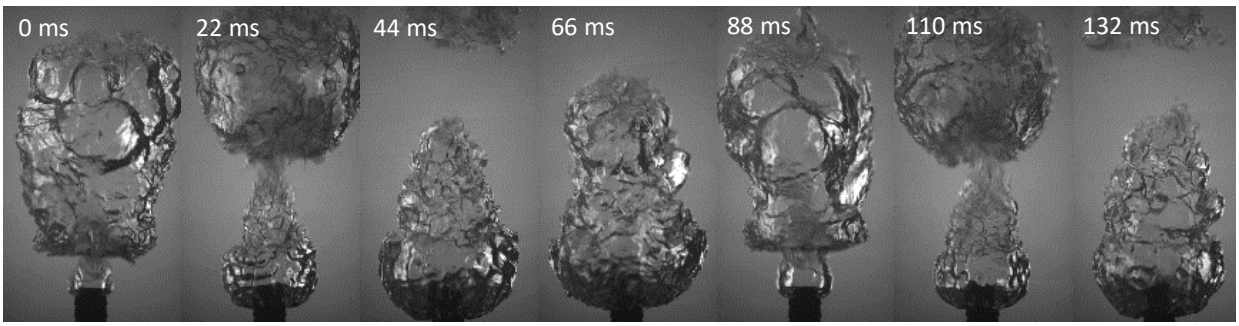

(g) 3.5 g/s

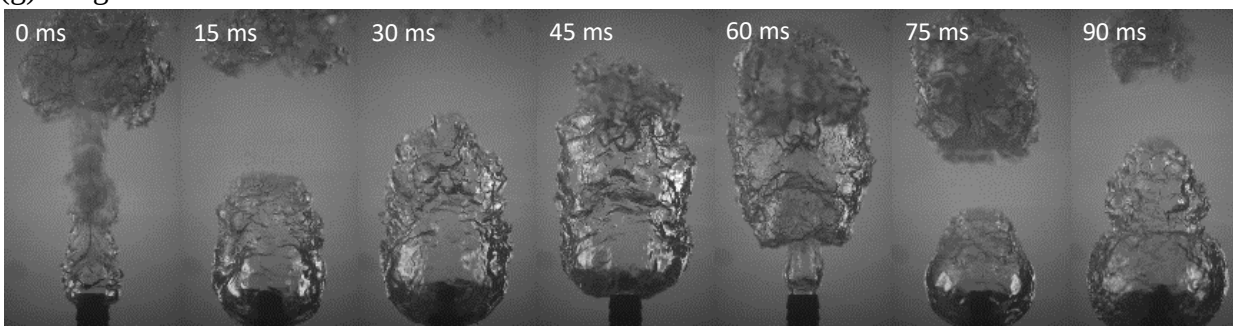

(h) 4.0 g/s

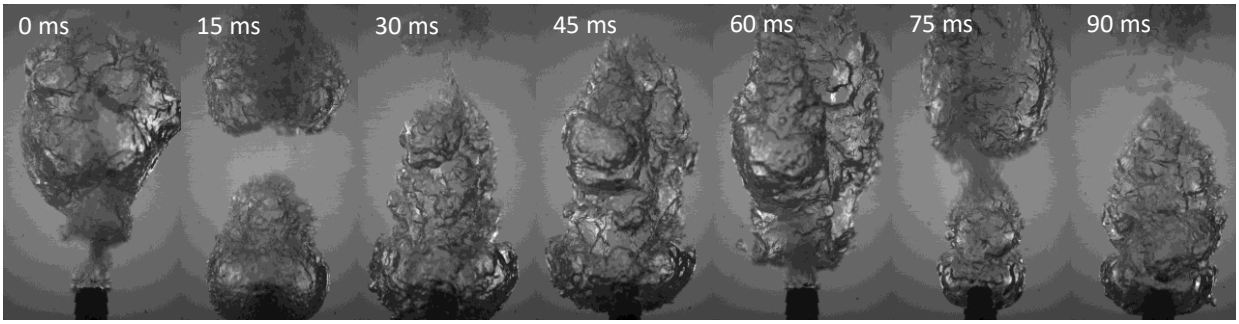
0 ms
15 ms
30 ms
45 ms
60 ms
75 ms
90 ms